HHS Public Access

Author manuscript

Nat Neurosci. Author manuscript; available in PMC 2018 June 19.

Published in final edited form as:

Nat Neurosci. 2017 August ; 20(8): 1062–1073. doi:10.1038/nn.4592.

Germline *Chd8* haploinsufficiency alters brain development in mouse

Andrea L. Gompers[1,2,^], **Linda Su-Feher**[1,2,^], **Jacob Ellegood**[3,^], **Nycole A. Copping**[1,4,^], **M. Asrafuzzaman Riyadh**[5,^], **Tyler W. Stradleigh**[1,2], **Michael C. Pride**[1,4], **Melanie D. Schaffler**[1,4], **A. Ayanna Wade**[1,2], **Rinaldo Catta-Preta**[1,2], **Iva Zdilar**[1,2], **Shreya Louis**[1,2], **Gaurav Kaushik**[5], **Brandon J. Mannion**[6], **Ingrid Plajzer-Frick**[6], **Veena Afzal**[6], **Axel Visel**[6,7,8], **Len A. Pennacchio**[6,7], **Diane E. Dickel**[6], **Jason P. Lerch**[3,9], **Jacqueline N. Crawley**[1,4], **Konstantinos S. Zarbalis**[5], **Jill L. Silverman**[1,4], and **Alex S. Nord**[1,2,*]

[1]University of California, Davis, Department of Psychiatry and Behavioral Sciences

[2]University of California, Davis, Department of Neurobiology, Physiology and Behavior

[3]The Hospital for Sick Children, Mouse Imaging Centre, Toronto, Canada

[4]University of California, Davis, MIND Institute, School of Medicine, Davis, CA

[5]University of California, Davis, Department of Pathology and Laboratory Medicine, Shriners Hospitals for Children, Institute for Pediatric Regenerative Medicine, Sacramento, CA

[6]Lawrence Berkeley National Laboratory, Functional Genomics Department, Berkeley, CA

[7]Department of Energy Joint Genome Institute, Walnut Creek, CA

[8]School of Natural Sciences, University of California, Merced, CA

[9]University of Toronto, Department of Medical Biophysics, Toronto, Canada

Summary

The chromatin remodeling gene *CHD8* represents a central node in neurodevelopmental gene networks implicated in autism. We examined the impact of germline heterozygous frameshift *Chd8* mutation on neurodevelopment in mice. *Chd8*$^{+/del5}$ mice displayed normal social interactions with no repetitive behaviors but exhibited cognitive impairment correlated with increased regional brain volume, validating that phenotypes of *Chd8*$^{+/del5}$ mice overlap pathology reported in humans with *CHD8* mutations. We applied network analysis to characterize neurodevelopmental gene expression, revealing widespread transcriptional changes in *Chd8*$^{+/del5}$ mice across pathways disrupted in neurodevelopmental disorders, including neurogenesis, synaptic processes and neuroimmune signaling. We identified a co-expression module with peak expression

*Corresponding author.

^These authors contributed equally

Author Contributions

A.L.G., L.S.-F., J.E., N.A.C. and M.A.R. are listed as joint first authors, as each led components of the experiments and analysis. A.L.G., L.S.-F., J.E., M.A.R., N.A.C., J.P.L., J.N.C., J.L.S., K.S.Z. and A.S.N. designed the experiments. Generation of mouse model: A.S.N., D.E.D., A.V., L.A.P., B.J.M., I.P.-F., V.A.; mouse behavior: N.A.C., M.C.P., M.D.S., J.N.C., J.L.S.; mouse MRI: J.E., J.P.L.; genomics and molecular genetics: L.S.-F., A.L.G., I.Z., A.A.W., R.C.-P., S.L., B.J.M., A.S.N.; neuroanatomy: A.L.G., M.A.R., T.W.S., I.Z., G.K., K.S.Z. A.L.G., L.S.-F., J.E., N.A.C., M.A.R., K.S.Z., J.N.C., J.L.S. and A.S.N. drafted the manuscript. All authors contributed to manuscript revisions.

in early brain development featuring dysregulation of RNA processing, chromatin remodeling and cell-cycle genes enriched for promoter binding by Chd8, and we validated increased neuronal proliferation and developmental splicing perturbation in *Chd8*$^{+/del5}$ mice. This integrative analysis offers an initial picture of the consequences of *Chd8* haploinsufficiency on brain development.

Introduction

DNA packaging determines the transcriptional potential of a cell and is central to the development and function of metazoan cell types[1]. Chromatin remodeling complexes control the local chromatin state, yielding either transcriptional activation or repression. Pluripotency, proliferation and differentiation are dependent on genomic regulation at the chromatin level, and proteins that control chromatin packaging are critical in development and cancer[2]. Although many chromatin remodeling factors function across organ systems, case-sequencing efforts have linked mutations of chromatin genes with specific, causal roles in neurodevelopmental disorders (NDDs)[3-6]. This finding is particularly strong for rare and *de novo* mutations in autism spectrum disorder (ASD)[7,8]. Understanding how mutations to chromatin remodeling genes affect transcriptional regulation during brain development may reveal developmental and cellular mechanisms driving NDDs.

A key gene that has emerged from studies profiling rare and *de novo* coding variation in ASD is the gene *CHD8*, which encodes the chromatin remodeler CHD8 (chromodomain helicase DNA-binding protein 8)[9]. In addition to ASD, human individuals harboring *CHD8* mutations exhibit macrocephaly, distinct craniofacial morphology, mild-to-severe intellectual disability (ID) and gastrointestinal problems[9]. Homozygous deletion of *Chd8* in mice is early embryonic lethal[10]. *Chd8* knockdown in zebrafish recapitulates macrocephaly and gastrointestinal phenotypes[9,11], suggesting a high degree of evolutionary conservation of CHD8 function in development. It has been proposed that CHD8 achieves this regulatory function in brain development by binding to relevant gene promoters and enhancers[11-14]. Although recent mouse studies indicate that *Chd8* is required in neurogenesis and that mutations to *Chd8* cause behavioral phenotypes[13,15], important questions remain regarding the role of Chd8 in regulating neurodevelopment, brain structure, and behavior via direct and indirect transcriptional regulation. Characterizing the functional impact of germline heterozygous *CHD8* mutation on brain development could reveal specific and generalizable mechanisms linking chromatin biology to NDD pathology. Toward this goal, we generated a novel germline 5-base-pair (bp) deletion in *Chd8* using CRISPR/Cas9 genome engineering and assayed neuroanatomic, behavioral, and transcriptional phenotypes associated with *Chd8* haploinsufficiency in the developing mouse brain.

Results

Mice harboring heterozygous germline Chd8 mutation exhibit megalencephaly

We used CRISPR/Cas9 targeting of C57BL/6N oocytes to generate mice harboring 5-bp or 14-bp deletions in *Chd8* exon 5, upstream of the majority of identified human mutations[9] (Figure 1A-1C). F0 mutation carrier lines were expanded via breeding to wild-type C57BL/6N (WT) mice. Heterozygous male mice were bred for at least four generations

before further experiments, and multiple litters were used for all experiments to eliminate potential off-target mutations. Consistent with an earlier study[10], the presumed *Chd8* frameshift alleles resulted in embryonic lethality in homozygous mutants, but heterozygous (*Chd8*$^{+/del5}$) mice were viable, reached a normal lifespan, and were fertile irrespective of sex.

We performed quantitative reverse-transcription PCR (qRT-PCR) and western blot analysis on brain lysates, using an N-terminus Chd8 antibody that has been used previously used for Chd8 chromatin immunoprecipitation followed by deep sequencing (ChIP-seq)[12]. Heterozygous mutation resulted in decreased *Chd8* transcript and protein at embryonic day (e)14.5, postnatal day (P)0, and in adults (Figures 1D-1E, S1A-1C). We identified a band representing full-length Chd8 (~280 kDa), which was consistently significantly reduced in *Chd8*$^{+/del5}$ mice at all stages (Figure S1A-C). We also observed a smaller, ~110 kDa band, similar in size to what has been reported as a short Chd8 isoform[13], which displayed inconsistent trends of lower expression in *Chd8*$^{+/del5}$ mice (Figure S1A-1C). We performed RNA-sequencing on e12.5 WT mice and matched littermates from both the 5-bp and 14-bp deletion lines (RNA-seq, described below), observing sequence reads overlapping the *Chd8* deletion in both 5-bp and 14-bp libraries but not in WT libraries. For both mutant lines, *Chd8* deletion reads occurred at lower frequencies relative to WT allele reads, suggesting the frameshift transcripts underwent degradation. For the majority of the following studies, we analyzed mice harboring the 5-bp deletion allele.

We tested for differences in brain size in *Chd8*$^{+/del5}$ mice at birth (P0), as macrocephaly is a hallmark trait in patients with *CHD8* mutations[9]. The maximal cortical anteroposterior length of *Chd8*$^{+/del5}$ brains was ~7% longer than matched wild-type (WT) littermates ($p < 0.0001$) with no substantial differences between sexes (Figure 1F). Whole-mount and Nissl-stained coronal brain sections were examined at P7 (Figure 1G), and no overt neuropathological anomalies were observed. No significant differences were observed in cortical thickness at 30% and 70% distance from the dorsal midline ($p = 0.224$ and $p = 0.268$, respectively), though brains of *Chd8*$^{+/del5}$ mice trended larger across both measurements (Figure 1H). The overall neocortical section area was ~8% larger in *Chd8*$^{+/del5}$ brains ($p = 0.0328$), driven predominantly by an increase in length ($p = 0.0026$), confirming cerebral megalencephaly at P7 (Figure 1H).

Behavioral phenotyping of adult Chd8$^{+/del5}$ mice

We performed a tailored behavioral battery using two standard assays each of cognitive, social and repetitive behaviors[16] in two independent cohorts of adult *Chd8*$^{+/del5}$ mice (first cohort: 9 male, 10 female; second cohort: 11 male, 11 female) and WT littermates (first cohort: 11 male, 10 female; second cohort: 11 male, 9 female; Figures 2 and S2). Learning and memory were evaluated using fear conditioning and novel object recognition. Fear conditioning evaluated memory for learned associations to an environmental context at 24 h and to an auditory cue at 48 h after training. *Chd8*$^{+/del5}$ mutant mice exhibited less freezing when placed in the context chamber compared to WT littermate controls (Figure 2A; $t_{(1, 37)} = 3.3492$, $p = 0.0019$). *Chd8*$^{+/del5}$ mutant mice also exhibited lower freezing scores to the auditory cue (Figure 2B; $t_{(1, 37)} = 2.7064$, $p = 0.0104$). WT littermates spent more time

exploring the novel object than the familiar object, whereas *Chd8*$^{+/del5}$ mutant mice failed to exhibit more novel object investigation (Figure 2C; WT: $F_{(1, 19)} = 11.5030$, $p = 0.0031$; *Chd8*$^{+/del5}$: $F_{(1, 18)} = 3.2825$, $p = 0.0867$), indicating deficits in recognition. Replication with a second, independent cohort of WT and *Chd8*$^{+/del5}$ mice similarly found deficits in contextual and cued conditioning and novel object recognition (Figure S2), indicating that *Chd8*$^{+/del5}$ mice exhibited deficits in learning and memory.

Behaviors relevant to diagnostic symptoms of ASD were assessed using corroborative assays of social and repetitive behaviors[17]. Normal sociability was detected in both genotypes (Figure 2D-2I). Time spent in the chamber with the novel mouse was greater than with the novel object, meeting the definition of sociability in this assay, for both WT and *Chd8*$^{+/del5}$ mice (Figure 2D; WT: $F_{(1, 19)} = 16.31$, $p = 0.0007$; *Chd8*$^{+/del5}$: $F_{(1, 18)} = 9.744$, $p = 0.0059$). No sex differences were detected ($F_{(1, 37)} = 2.16$, $p = 0.149$). Time spent sniffing the novel mouse was greater than time spent sniffing the novel object in both WT and *Chd8*$^{+/del5}$ (Figure 2E; WT: $F_{(1, 18)} = 7.00369$, $p = 0.0164$; *Chd8*$^{+/del5}$: $F_{(1, 17)} = 12.8051$, $p = 0.0023$), with no sex differences ($F_{(1, 35)} = 0.0985$, $p = 0.7555$). The number of entries into the side chambers was not affected by genotype in the social phase (Figure 2F; $F_{(1, 37)} = 0.11$, $p = 0.73$), nor in the habituation phase ($F_{(1, 37)} = 0.30$, $p = 0.584$), indicating normal exploratory activity in both genotypes during the assay. No deficits were observed in social parameters in male *Chd8*$^{+/del5}$ mice during male-female reciprocal social interaction (Figure 2G-2I). WT and *Chd8*$^{+/del5}$ males spent similar amounts of time sniffing (Figure 2G; $t_{(1, 17)} = 0.9409$, $p = 0.3599$), and following (Figure 2H; $t_{(1, 17)} = 0.5785$, $p = 0.5705$) the estrous WT female. Ultrasonic vocalizations during male-female interaction showed no genotype difference in number of emitted calls (Figure 2I; $t_{(1, 17)} = 0.1634$, $p = 0.8722$). No spontaneous stereotypies or repetitive behaviors were observed in the self-grooming assay (Figure 2J; $t_{(1, 38)} = 0.8552$, $p = 0.3978$) or numbers of marbles buried (Figure 2K; $t_{(1, 38)} = 1.0151$, $p = 0.3165$). No sex differences were detected (self-grooming: $t_{(1, 36)} = -0.504$, $p = 0.619$; marble burying: $t_{(1, 38)} = 1.4883$, $p = 0.1449$). Open-field locomotor activity did not differ between genotypes (Figure 2L, $t_{(1, 38)} = 1.1795$, $p = 0.2455$), indicating normal exploratory and motor abilities. No substantial differences were observed in body weight or other relevant measures of general health in adult *Chd8*$^{+/del5}$ mice.

Analysis of Chd8$^{+/del5}$ adult brain structure via MRI

Intact brains were collected from the same mice that comprised the first cohort of behavioral phenotyping. Structural MRI was performed to identify changes in absolute (mm^3) and relative regional brain volume and connectivity. In regional analysis, cortex was most affected, with a 7.5% increase in absolute volume in *Chd8*$^{+/del5}$ mice (false discovery rate (FDR) = 1%). Similarly, cerebral white matter and cerebral gray matter were larger in *Chd8*$^{+/del5}$ mice at 5.4% (FDR = 3%) and 6.1% (FDR = 2%), respectively. We assessed 159 independent brain regions with divisions across the cortex, subcortical areas, and cerebellum (full results reported in Table S1). *Chd8*$^{+/del5}$ mice showed robust increases in absolute volume across cortical regions, hippocampus (+10.3%, FDR < 1%) and amygdala (+11.0%, FDR < 1%, Figure 3A). After correction for total brain volume, relative volumes were still significantly larger, though cortex failed to surpass the FDR < 5% cutoff (Figure 3B). *Chd8*$^{+/del5}$ mice also displayed increased cortical thickness, particularly along the cingulate

cortex (Figure 3C). Deep cerebellar nuclei showed decreased relative volume (-1 to -3%, FDR < 0.3%). Voxel-wise differences showed similar trends (Figure 3D). Diffusion tensor imaging revealed no significant differences in fractional anisotropy or mean diffusivity in either the regional or voxel-wise measurements, indicating that white matter organization and long-range connectivity in *Chd8*$^{+/del5}$ mice was not grossly different from that in WT littermates (Figure S3).

Performing behavioral and structural MRI analyses on the same set of mice allowed us to test correlations between brain volume and behavioral performance. Increased absolute volume of cerebral cortex (f-stat = 33.6, FDR < 0.1%), hippocampus (f-stat = 29.0, FDR < 0.1%) and amygdala (f-stat = 38.6, FDR < 0.1%) were correlated with deficits in learning and memory as assessed by the context fear conditioning task (R^2: cortex = 0.1855, hippocampus = 0.148, amygdala = 0.1352) (Figure 3E). This relationship was driven by *Chd8*$^{+/del5}$ mice with increased brain volume. Similar correlations were present between other brain regions and cued and context responses, suggesting that the correlation between fear conditioning performance and brain volume was a general rather than region-specific relationship.

Differential gene expression across neurodevelopment in Chd8$^{+/del5}$ mice

We applied RNA-seq in forebrain dissected from four developmental stages (e12.5, e14.5, e17.5, and P0) and adult mice (age >P56) (Figure 4A). This strategy was designed to capture changes during embryonic neurodevelopment, but has decreased sensitivity for changes limited to postnatal or adult brains. After quality filtering, we analyzed 26 *Chd8*$^{+/del5}$ and 18 WT littermates (sample details in Table S2). Using a statistical model that accounted for sex, developmental stage and sequencing batch, we tested for differential expression across 11,936 genes that were robustly expressed in our data sets. At significance cutoffs corresponding to FDR < 0.05 (p < 0.0021), FDR < 0.1 (p < 0.0088) or FDR < 0.20 (p < 0.0369), we found 510, 1,040, and 2,195 genes, respectively, that were differentially expressed (DE) (Table S3).

The majority of significant expression changes in *Chd8*$^{+/del5}$ were relatively small (99.5% < 1.5 absolute fold change across stages, Figure 4B), indicating that changes in neurodevelopmental gene expression were widespread yet subtle. The top DE gene was *Chd8* (log2 fold change = 0.59, p = 2.20E-27, FDR = 3.18E-23). *Chd8* expression declined across development, with substantial reductions in *Chd8*$^{+/del5}$ mice at each stage (Figure 4C). We validated expression changes at P0 for a set of genes via qRT-PCR (Figure S4, primers are listed in Table S4), including *Hnrnpa2b1*, for which we additionally validated differential protein levels in P0 *Chd8*$^{+/del5}$ forebrain (Figure 4D-4E). Gene set enrichment analysis of Gene Ontology (GO) terms and Reactome[18] pathways identified strong enrichment among DE genes for annotations associated with RNA processing, chromatin remodeling, and cell cycle, with numerous additional annotations enriched at lower levels (Table S5-S6). Similar enrichment was observed for DE genes at FDR cutoffs of 0.05, 0.10, and 0.20.

To identify direct regulatory targets of Chd8, we used ChIP-seq to map regions of Chd8 genomic interactions in adult mouse forebrain. After merging two independent samples with

similar binding patterns, we identified 708 peaks using stringent enrichment criteria (Figure 4F, Table S3). Chd8 binding occurred nearly exclusively at gene promoters in our adult forebrain data set. We observed strong concordance in enriched functional annotation terms between DE and Chd8-bound genes (Figure 4G). While the majority of DE genes did not exhibit Chd8 binding in the adult forebrain Chd8 ChIP-seq generated here, we observed strong enrichment for binding among downregulated genes (Figure 4I). In contrast, we found no enrichment among upregulated DE genes for Chd8 promoter binding. We did not find evidence of a primary sequence motif in Chd8 ChIP-seq peak regions, suggesting indirect genomic recruitment, but found weaker, yet significant, enrichment of secondary motifs such as YY1, (e-value = 4.2×10^{-31}), NRF1, (e-value = 8.5×10^{-24}), and NFYB (e-value = 1.3×10^{-17}) (Figure S5A).

In agreement with other studies of transcriptional changes associated with reduction of *Chd8* expression[11,12], autism risk genes such as *Kdm5b* and *Bcl11a* were DE in *Chd8*$^{+/del5}$ mice (Figure 4D). We tested for overlap between DE downregulated and upregulated genes (FDR < 0.20) and published gene sets relevent to autism genetics and *Chd8* regulation. Of 141 ASD risk genes based on case mutations[19] expressed in our data, 37 were DE at FDR < 0.20 and downregulated, representing strong enrichment (permutation test, $p = 2.8 \times 10^{-10}$) (Figure 4H). We similarly observed enrichment among down-regulated DE genes with autism risk genes identified by other studies[20,21] (Figure 4I) and with FMRP (Fragile × mental retardation protein) targets[22] (p = 0.04). Finally, we observed enrichment (p = 0.012) between DE upregulated genes and genes associated with immune response that were upregulated in cortex from postmortem ASD brains[23,24]. We did not identify enrichment with genes downregulated in postmortem ASD cortex.

Next, we asked whether our DE data was consistent with differential expression in independent studies of *Chd8* mutation or knockdown[11-13,15]. We observed consistent enrichment among up- and downregulated DE genes in *Chd8*$^{+/del5}$ forebrain and up- and downregulated DE genes identified in previous studies (Figure 4J). We also used the same methods used here to reanalyze neurodevelopmental RNA-seq data from independent studies of germline heterozygous *Chd8* mutation[13] and *in utero* knockdown via *Chd8* shRNA delivery to e14.5 brain ventricle[15] (Figure S5B-S5C and Table S3). *Chd8* was more strongly downregulated in the knockdown model[15], and upregulated in the independent *Chd8* mouse model[13]. Nonetheless, we observed significant overlap between genes identified here and in the other two studies (Figure 4J). For overlapping DE genes from our data and the other two studies, DE sensitivity and effect sizes were generally larger in the knockdown data[15] and smaller in the independent germline model[13] compared to our data (Figure S5B-S5C), suggesting differences in transcriptional consequences after knockdown and across different alleles or genetic backgrounds. We noted a reversal in direction of some specific DE effects in the knockdown data versus our data, including for neuronal differentiation genes (downregulated here but upregulated after knockdown), further suggesting differential impact of knockdown versus germline mutation.

We next explored how DE genes are organized into expression trajectories during brain development toward identifying perturbation to stage-specific processes. We used weighted gene co-expression network analysis (WGCNA[25]) to identify five discrete expression

trajectory modules across forebrain development (Figure 5A-5C and Table S7). DE genes assigned to specific modules were enriched for stage-specific annotation terms (Figure 5D and Table S5). Two modules (M.1 and M.3) were enriched for downregulated genes while the other three modules (M.2, M.4, and M.grey) were enriched for upregulated genes (Figure 5E). M.1, characterized by decreasing expression across neurodevelopment, is strongly associated with chromatin organization, RNA processing and cell cycle regulation, and it included the largest number of DE downregulated autism risk genes (Figure 5F). M.1 was the only module enriched for targets of Chd8 binding. M.1 downregulated DE genes overlapped genes in early expressed ASD-relevant networks[26] (Parikshak.DEV.M2 and Parikshak.DEV.M3; Figure 5G). M.2 was characterized by early low expression that gradually increased. Downregulated genes in M.2 were enriched for FMRP targets[22], GO and Reactome terms that are hallmarks of mature neurons (Tables S5-S6), and include synaptic genes (Figure S5D) and autism risk genes such as *Cers4* and *Gria1*. DE genes from M.2 were enriched for later developmental ASD-relevant modules[26] (Parikshak.DEV.M13, Parikshak.DEV.M16, and Parikshak.DEV.M17) linked to synaptic developmental and homeostatic processes, consistent with developmental timing (Figure 5G). M.3 genes exhibited rising expression from e12.5 to P0, with lower expression in adult brain, were enriched for GO terms associated with transient development processes (for example, axon guidance) and include autism risk genes involved in neuronal maturation (for example, *Bcl11a)*. Compared to genes identified as DE in postmortem ASD cortex[24], we identified enrichment with two modules characterized by increased expression of genes linked to immune function and cell identity of astrocytes (Parikshak.ASD.M9, enriched for upregulated genes in our M.2 and M.4) or microglia (Parikshak.ASD.M19, enriched for upregulated genes in our M.1; Figure 5G). These results show that the impact of *Chd8* haploinsufficiency reaches across stages and biological processes.

We further focused on M.1, which showed the strongest enrichment for autism risk early developmental modules[26] and for Chd8 binding targets in mouse brain (Figure 5F-5G). M.1 showed a general trend of decreasing expression (Figure 6A), had the greatest number of DE genes and was significantly enriched for downregulated genes ($p = 8.8 \times 10^{-26}$). We found 865 genes in M.1 that were DE at FDR < 0.20 (641 downregulated, 224 upregulated), accounting for ~39% of all DE genes identified in our study. Upregulation of M.1 genes peaked at e14.5; downregulation peaked from e14.5 to e17.5 (Figure 6B). Analysis of protein-protein interactions (STRING[27]) showed that DE (FDR < 0.10) genes in M.1 had more interactions than expected by chance (observed edges = 1,479, expected edges = 512, enrichment = 2.89, STRING $p < 0.0001$). Interacting genes in M.1 were enriched for GO terms including RNA processing, chromatin modification, and cell cycle (Figure 6C). While protein-protein interaction databases have biases, these results highlight interconnectedness among these three processes at the level of Chd8 regulation and gene expression. M.1 DE genes include 38 autism-relevant genes, including many annotated to the highlighted GO terms (Figure 6D).

Increased prenatal proliferation of neural progenitors in Chd8$^{+/del5}$ mice

To examine whether alterations in developmental genes play a functional role in neuronal development that could lead to megalencephaly, we performed 5-ethynyl-2′-deoxyuridine

(EdU) proliferation assays at e13.5. After a 1.5 h pulse, we observed a 15.9% increase in EdU^+ cells in the germinal cortical ventricular and subventricular zones (VZ and SVZ, respectively) of mutant animals ($p = 0.0388$; Figure 6E), indicating perturbed neurogenesis in the *Chd8*$^{+/del5}$ mutants. Additionally, since a number of genes associated with brain development and cortical structure were DE, we examined the cortical cytoarchitecture via analysis of layer-specific markers Tbr1, Ctip2 and Brn2 by immunostaining at P0 and P7 (Figure S6). We observed no gross alterations to lamination and found no evidence for focal cortical lesions. To further delineate proliferative changes in *Chd8*$^{+/del5}$ mice, we assessed neural progenitor populations at e14.5 (Figure 7). First, we examined $Pax6^+$ radial glial cells, measuring VZ area over the entire cortical hemisphere. The VZ in *Chd8*$^{+/del5}$ embryos was significantly increased by ~18% (Figure 7A and 7E, $p = 0.0165$). We observed a ~26% increase in $Pax6^+$ cells in *Chd8*$^{+/del5}$ brains (Figure 7B and 7F, $p = 0.0032$). Subsequently, we labeled $Tbr2^+$ intermediate progenitors, observing a significant decrease by ~24% in *Chd8*$^{+/del5}$ mice (Figure 7C and 7G; $p = 0.0086$), indicating different proliferative trajectories for these two progenitor types. Finally, we performed pulse-chase assays to determine the quit (Q) fraction of cortical cells exiting the cell cycle over a defined 20 h using the proliferation marker Ki67. $EdU^+/Ki67^-$ cells were significantly increased, corresponding to an increase in Q-fraction by ~25% in *Chd8*$^{+/del5}$ embryos (Figure 7D and 7H; $p = 0.0057$). These results that indicate alteration to cortical projection neuron production may represent a cellular substrate for megalencephaly in *Chd8*$^{+/del5}$ mice.

Neurodevelopmental RNA processing is perturbed in Chd8$^{+/del5}$ mice

Downregulated DE genes with divergent expression trajectories were significantly overrepresented among genes annotated to RNA processing and mRNA splicing in the Reactome database (Figure 8A-8B and Table S6). For example, *Dhx9* (M.1) decreases across neurodevelopment and has not been functionally characterized in brain but has been reported in autism-risk networks[20], while *Upf3b* (M.3) expression increases across development and is a neuron-specific factor required during neuronal differentiation that is implicated in ID[28,29]. We examined whether *Chd8*$^{+/del5}$ mice exhibited aberrant splicing during brain development linked to DE of RNA processing genes. We used the Mixture of Isoforms (MISO[30]) program to examine our RNA-seq data for differential splicing (DS) between WT and *Chd8*$^{+/del5}$ mice and across neurodevelopment in WT mice (Table S8). Genes associated with a DS event in *Chd8*$^{+/del5}$ mice significantly overlapped downregulated ($p = 1.2 \times 10^{-10}$) but not upregulated DE genes, raising the possibility that splicing changes explain some proportion of differential expression (Figure S7A). DS genes identified in *Chd8*$^{+/del5}$ mouse brain were enriched for DS-associated genes identified in postmortem ASD cortex[24] ($p = 1.2 \times 10^{-17}$), suggesting that DS in *Chd8*$^{+/del5}$ mice is linked to ASD-relevant DS (Figure S7A).

At e17.5, MISO identified 591 DS events between WT and *Chd8*$^{+/del5}$ mice, of which 393 (~66%) were also DS between e14.5 WT and e17.5 WT mice (Figure 8C). These results suggest that differential splicing between WT and *Chd8*$^{+/del5}$ mice was linked to developmental changes in splicing. To investigate this, we examined correlation between DS events present in both e14.5 WT versus e17.5 WT and e17.5 *Chd8*$^{+/del5}$ versus e17.5 WT comparisons. Percentage spliced in (PSI) values of DS events identified in the e17.5

Chd8$^{+/del5}$ versus e17.5 WT comparison correlated positively with PSI values in the e14.5 WT versus e17.5 WT comparison (Figure 8D). This correlation suggests DS in e17.5 *Chd8*$^{+/del5}$ mice corresponds to an intermediate developmental state between WT e14.5 and e17.5. We validated developmentally relevant *Chd8*$^{+/del5}$ DS using a known neurogenic splicing event, inclusion or exclusion of a ~6-kb *Ank2* exon[31]. Inclusion of the *Ank2* exon increased between e12.5 and e17.5 in WT (Figure 8E), consistent with expectations[31]. qRT-PCR analysis of the *Ank2* exon validated the exon inclusion increase across development in WT and the decrease from e17.5 WT levels in e17.5 *Chd8*$^{+/del5}$ mice (Figure 8F). We also validated developmental splicing changes in *Srsf7* detected via MISO analysis (Figure S7B). Our results suggest that perturbed splicing in *Chd8* haploinsufficiency may contribute to the neurodevelopmental phenotypes in *Chd8*$^{+/del5}$ mice.

Discussion

Modeling how constitutive heterozygous germline mutations impact mammalian brain development is critical to understanding the neurobiology of disorders like ASD and ID, which are strongly associated with single copy loss-of-function mutations. After validation that germline 5-bp and 14-bp deletion mutations in *Chd8* exon 5 resulted in haploinsufficiency, we present here an initial integrative picture of the consequences of *Chd8* haploinsufficiency on neurodevelopment. The presence of genomic and neuroanatomical phenotypes in our *Chd8*$^{+/del5}$ mice paralleled the clinical signature of human *CHD8* mutations, suggesting similar neurodevelopmental pathologies between species. Our study revealed NDD-relevant phenotypes and mechanistic insights into why haploinsufficiency of a general chromatin factor produces neurodevelopmental phenotypes.

We report behavioral outcomes in our heterozygous *Chd8*$^{+/del5}$ mice, specifically learning and memory impairments, but no atypical sociability or repetitive behaviors. There are three recent publications associated with downregulation of *Chd8* in mice. Durak et al. 2016[15] reported an in utero knockdown of *Chd8* expression, including restricted knockdown of *Chd8* in upper cortical layer neurons. Katayama et al. 2016[13] generated two lines of *Chd8* mutant mice via embryonic stem cell targeting, while Platt et al. 2017[14] used CRISPR/Cas9 targeting to generate indel mutations in *Chd8*. The obvious differences in biological consequences and mechanisms between in utero knockdown[15] and our germline heterozygous model likely explain many differences and make cross-approach comparisons a challenge. Our data on the absence of repetitive behaviors agree with those reported in Katayama et al. 2016[13] and Platt et al. 2017[14]; however, these studies also report specific social phenotypes in heterozygous *Chd8* mice. We focus our comparison on the Katayama et al.[13] study as we were able to directly compare neurodevelopmental gene expression changes to our model. We observed differences in strength of expression changes that may be due to allele or genetic background. Katayama et al.[13] report phenotypes relevant to social deficits, but report normal acquisition learning using the Barnes and T-maze assays. Discrepancies in cognitive phenotypes could be attributed to the tasks conducted, since spatial maze tasks are primarily hippocampal-dependent, while components of fear conditioning and novel object recognition require other brain regions including amygdala. Additionally, our *Chd8*$^{+/del5}$ mutation was generated and maintained on a C57BL/6N background, while Katayama et al.[13] harbored a different mutation on C57BL/6J.

Background strain differences in behavioral phenotypes are common and C57BL/6N generally show higher basal freezing during contextual fear freezing, which allows for a larger signal and detection of genotype differences[32].

Our finding of normal sociability is consistent with results reported for other *Chd8*$^{+/-}$ germline models[13,14]. However, both other models[13,14] report abnormalities in social behavior based on failure of *Chd8*$^{+/-}$ mice to exhibit preference for social novelty between a novel and familiar mouse. Preference for social novelty is dependent on olfactory discrimination, which is driven by a variety of sensory and processing systems. As such, the combination of normal three-chamber assay sociability but failure to discriminate a novel mouse in these models[13,14] could represent mild deficits in social interaction or could be due to other factors impacting olfactory discrimination. Another difference is that Katayama *et al.*[13] tested only male mice with a broad age range of 12–50 weeks of age, while our battery was conducted using both sexes at younger ages, between 6–16 weeks, to avoid aging as a confounding variable. We also note that several studies of other mouse models with mutations in genes implicated in ASD have not identified deficits in social behaviors[33], potentially due to evolutionary divergence between mouse and human neurobiology, allele or genetic background differences, or sensitivity of methods used to evaluate ASD-relevant behavior in mice.

The structural changes in the brain of adult *Chd8*$^{+/del5}$ mice observed here parallel those found in other relevant mouse models. A recent study examined 26 different mouse models related to autism[34], clustering these models into three distinct groups. Key aspects of Group 1 included larger cortical structures, particularly the frontal and parietal lobes, and smaller structures in the cerebellum, which is in line with the *Chd8*$^{+/del5}$ mouse described here. This group of models included *Nrxn1α*, *Shank3, En2* and *Fmr1* mutants. The *Chd8*$^{+/del5}$ mouse most resembled the differences found in the *Fmr1* mutant mice. Further examination may reveal similarities with other mouse models within this group beyond neuroanatomy (for example, excitatory deficits in the *Nrxn1α* mouse[35]), as suggested by the widespread transcriptional changes present in *Chd8*$^{+/del5}$ neurodevelopment. Increases in cortical anteroposterior length and developmental neurogenesis appear largely overlapping in *Chd8*$^{+/del5}$ mice and *Wdfy3* mutants, another model of megalencephaly in ASD[36]. Future work will be needed to test for causal relationships between structural changes and behavior in *Chd8*$^{+/del5}$ mice.

Our RNA-seq analysis captured subtle changes in transcription across brain development in *Chd8*$^{+/del5}$ mice, as well as evidence of differential splicing. Differential expression changes were consistent across developmental stages for perturbed genes highly relevant to ASD-associated networks and strongly correlated with biological pathways and expression modules of interest. Our network analysis, using *in vivo* data, enabled characterization of the impact of *Chd8* haploinsufficiency across neurodevelopment at a level of detail sufficient to capture perturbations across developmental stages and processes. Our results indicate convergent neuropathology connecting principle gene networks identified in ASD case sequencing studies, particularly chromatin remodeling, neuronal differentiation and synaptic pathways[7,8], and those identified in other ASD-relevant pathways such as immune response[24] and FMRP binding[22]. Our findings suggest a hierarchy of changes in *Chd8*$^{+/del5}$

brain development anchored by dysregulation of genes in M.1, which represents a highly interactive network central to control of chromatin state, RNA processing, and cell cycle, including numerous genes implicated in ASD. Among these genes, our results suggest direct role and requirement for WT *Chd8* expression levels in activating target gene expression. As seen with other NDD genetic models such as *Fmr1*[37] and *Rbfox1*[38], disruption to RNA processing, likely driven by indirect transcriptional regulation here, appears to be an important player in *Chd8*$^{+/del5}$ neuropathology. Further studies are needed to capture neuroanatomical and cellular changes associated with differential expression signatures and to determine stage- and cell-specific patterns and roles of Chd8 binding. This is especially critical given that contrasting Chd8 genomic interaction patterns have been reported in brain[11-14].

We report overall increased proliferation during the peak window of embryonic neurogenesis, with different consequences for the progenitor populations involved. The observed overall increase in proliferation in our experiments contrasts with the decreased proliferation reported in an in utero *Chd8* knockdown model[15]. These differences could be explained by the timing of in utero knockdown at e14.5 (after initial symmetric expansion of the radial glia pool), by the presence of non-cell-autonomous effects or due to differences in proliferation assay timing. Time-point-specific analysis of cell cycle, proliferation and apoptosis will be needed to understand the comprehensive impact of *Chd8* haploinsufficiency on cell populations in the brain. It is possible that contrasting outcomes are due to differences in *Chd8* dosage, considering that knockdown resulted in greater *Chd8* downregulation[15]. As complete *Chd8* loss impedes embryonic development at very early stages[10], downregulation beyond haploinsufficiency may interfere further with developmental cellular pathways. In support of this, neuronal development genes down-regulated in our M.3 module were upregulated after *in utero* knockdown, suggesting that knockdown caused an early shift from proliferation to differentiation[15] that did not appear to occur with heterozygous germline mutation.

Our initial survey of mice heterozygous for mutation to *Chd8* revealed significant findings across genomic, anatomical, and behavioral axes of neurobiology. Our experiments link cognitive deficits, increased regional brain volume, and perturbations of biological pathways across neurodevelopment, recapitulating traits observed in human individuals that carry mutations in *CHD8*. The transcription data generated here represent a resource for dissecting the pathways involved in NDD pathogenesis and for prioritizing risk genes from genetic studies. Additional studies will be necessary to replicate and compare findings across mutant *Chd8* alleles and genetic backgrounds and to clarify dosage-specific phenotypes. Our results offer insight into neurodevelopmental pathology associated with mutations to *CHD8*, a genetic model that appears to be a bellwether for mutations affecting chromatin remodeling in autism.

Methods

Generation of Chd8 mutant mice

We used Cas9-mediated mutagenesis of C56BL/6N oocytes to generate two mouse lines harboring frameshift deletions (5-bp and 14-bp) in mouse *Chd8* exon 5. Guide RNA was

designed and synthesized according to described methods[39], and pooled with Cas9 mRNA and injected into mouse oocytes. We scanned the *Chd8* coding sequence for unique gRNA target sites, identifying one in exon 5 with sequence GAGGAGGAGGTCGATGTAAC. This sequence maps uniquely to the target site via BLAT (mm9), reducing the likelihood of off-target mutations. Initial Cas9 targeting was performed at Lawrence Berkeley National Laboratory. F0s (induced on C57BL/6N background) carrying mutations were genotyped and bred to expand lines that harbored a mutation. We identified F0 pups carrying 5-bp (mm9: chr14:52,847,259-52,847,263) and 14-bp deletions (mm9: chr14:52,847,249-52,847,262) in *Chd8* exon 5 that overlapped the target sequence. The deletions occur at position 1,814 (5-bp deletion) or 1,813 (14-bp deletion) of *Chd8* mRNA (uc007tot.1). Both alleles match wild-type Chd8 amino acid sequence through position 604, after which the 5 bp and 14 bp deletion frameshifts are predicted to result in 16 and 14 altered amino acids, respectively, before a stop codon is reached. The full-length Chd8 protein is predicted to be 2,582 amino acids. Both deletion alleles are predicted to result in nonsense-mediated decay based on reduced frequency of mutant transcripts and decreased Chd8 protein levels. Deletion alleles were subcloned to verify DNA changes and genotyping was performed using allele-specific PCR with sequence verification.

The colony of animals carrying the 5-bp *Chd8* deletion allele was rederived at UC Davis and maintained by crossing male carriers with C57BL/6N wild-type females (Charles River). Extensive crossing of heterozygous mutation carriers to wild-type animals vastly reduces the likelihood that any potential off-target mutations caused by Cas9 targeting would persist in our mutant *Chd8* line. Genotypes were identified via allele-specific PCR and sequence-verified for all animals included in analyses, with the primers reported in Table S4. We examined Chd8 protein and transcript levels via western blot and qRT-PCR at e14.5 and P0 and compared cortical length in whole-mount P0 brains from $Chd8^{+/del5}$ mice and matched WT littermates. For all experiments, samples from both males and females were used unless otherwise described. All mouse studies were approved by the Institutional Animal Care and Use Committees at the University of California Davis and the Lawrence Berkeley National Laboratory. Subject mice were housed in a temperature-controlled vivarium maintained on a 12-h light-dark cycle. Efforts were made to minimize pain and distress and the number of animals used.

qRT-PCR

Differential expression of selected gene targets was verified by qRT-PCR at P0, using cDNA libraries prepared following the same protocols listed in ‘Genomics’. Primers are reported in Table S4. For qRT-PCR analysis, n = 9 wild-type and 7 $Chd8^{+/del5}$ forebrains from male and female samples were used. Samples were excluded if technical replicates failed. Cycle counts were normalized to *ActB*. Unpaired t-tests were performed on normalized relative gene expression between WT and $Chd8^{+/del5}$ brains using ΔΔCT. To reduce noise, the highest and lowest values from both groups were discarded. To validate differential splicing, we used isoform-specific quantitative reverse-transcription PCR on cDNA libraries prepared from forebrains dissected from $Chd8^{+/del5}$ and matched WT littermates. We used validated primers for isoform analysis of *Ank2* expression during development[31] and designed primers specific to a differentially spliced exon of *Srsf7*. Comparisons of splicing across

stages and between *Chd8*$^{+/del5}$ and matched WT littermates were analyzed using Welch's t-test and linear regression.

Western blot analysis

Isolated forebrain from e14.5 embryos (male and female littermates), P0 neonates, and P60 adults were lysed in 50 mM Tris HCl pH 8, 140 nM NaCl, 1 mM EDTA, 10% glycerol, 0.5% NP40 and 0.25% Triton with protease inhibitor cocktail (Roche). After sonication, samples were spun down and the supernatant was used for a BCA Bradford assay using the Spectramax 190 plate reader to assess protein concentration using a standard curve. We ran 22 μg of protein on a 3-8% Tris Acetate gel using the Novex western blotting system (Invitrogen). Anti-Chd8[12] (1:1,000, ab114126; Abcam), anti-Hnrnpa2b1[40] (1:1,000, ab31645; Abcam), and anti-Gapdh[41] (1:10,000, G8795; Sigma-Aldrich) primary antibodies were incubated overnight in Fluorescent Blocker solution (Millipore), visualized using a LI-COR Odyssey CLx system and quantified in FIJI (National Institutes of Health). For Chd8 western blots, both males and females were used. For the Hnrnpa2b1 western blot, only male samples were used. Protein levels assayed via western blot were compared via Student's t-test and one-way ANOVA for adult Chd8 levels.

Analysis of cortical length at P0

For gross anatomical measurements at P0 and P7, *Chd8* male and female littermates were decapitated and heads placed in 4% PFA for at least 24 h. Brains were carefully dissected and placed in an agarose mold to ensure specific positioning. Whole mount images were taken with the Zeiss Lumar.V12 stereoscope with a Ned Lumar .8 × FwD 80-mm objective and Axiovision 4.8 software. Analysis of cortical length measurements was performed with FIJI software (National Institutes of Health).

Morphological analysis

All histological experiments were performed at least in triplicate on embryos/pups from at least two separate litters. Following anesthesia, P7 male and female mice were transcardially perfused with 4% paraformaldehyde (PFA) in phosphate-buffered saline (PBS), followed by overnight fixation in the same solution. After fixation, brains were removed from the skull, embedded in 2% LTE Agarose/PBS and cut coronally in 50-μm sections on a vibratome (VT 1000S, Leica). Subsequently, the sections were mounted on glass slides (SuperFrost Plus, Thermo-Fisher), Nissl-stained with a 0.1% cresyl violet solution, and mounted with DePeX (Electron Microscopy Sciences, Hatfield, PA). Select sections, approximately corresponding to adult bregma −2 mm, were aligned across genotypes using subcortical anatomical landmarks for orientation (hippocampal length, thalamic size), and images of entire hemispheres were acquired on a Keyence BZ microscope. We measured individual morphological parameters using the Keyence BZ analyzer (hemispheric/neocortical circumference, neocortical thickness) or FIJI software (cortical area). Hemispheric circumferences were measured from the dorsal to the ventral midline. Neocortical circumferences were measured from the dorsal midline to a line perpendicular to the midline originating from the dorsal endpoint of the dorsal endopririform nucleus.

EdU labeling, and immunofluorescent analysis

Litters for neuroanatomy analysis were generated by breeding male *Chd8*$^{+/del5}$ mice with WT females. Brains were perfused before isolation, embedding and sectioning. Experimenters were blinded to genotype. Both male and female samples were used in the following assays. *EdU labeling and immunofluorescent analysis:* Time-pregnant females were intraperitoneally injected at e13.5 with 50 mg/kg body weight EdU. After 1.5 h (proliferation assay) or 20 h (Q-fraction analysis), females were anesthetized and embryos transcardially perfused with 4% PFA/PBS. After 2 h of further fixation in the same solution, embryo brains were immersed in 15% and then 30% sucrose in PBS, placed in OCT compound (Fisher HealthCare, Houston, TX), frozen in dry-ice-chilled methanol and sectioned at 16 μm (1.5-h pulse) or 18 μm (20-h pulse) on a cryostat (Leica Biosystems, Buffalo Grove, IL). EdU detection was performed with the Click-iT EdU Alexa Fluor 594 imaging kit protocol (Life Technologies, Carlsbad, CA) according to the manufacturer's instructions. Q-fraction analysis followed previously established practices[36]. In brief, midcortical 200-μm-wide segments were imaged and EdU^{+}/Ki67^{-} cells positioned basal to the SVZ counted, followed by the count of all EdU^{+} cells. The ratio of the two counts represented the Q-fraction. One sample each from WT and Chd8$^{+/del5}$ was removed from Q-fraction analysis due to difficulties in selecting the VZ. All immunolabeling was carried out on slide-mounted cryosections (18 μm) following standard protocols and using primary antibodies directed against Pax6[42] (PRB-278P-100; rabbit, 1:100, Covance, Princeton, NJ), Tbr2 (http://www.abcam.com/TBR2--Eomes-antibody-EPR19012-ab183991.pdf) (ab183991; rabbit, 1:400, Abcam, Cambridge, United Kingdom), or Ki67[43] (#12202; rabbit, 1:200, Cell Signaling, Danvers MA). Alexa Fluor secondary antibodies (488 and 594) were used at 1:200 concentrations (Thermo Fisher Scientific, Waltham, MA). All quantifications of labeled cells were carried out at equivalent anteroposterior positions between genotypes. To determine the dorsoventral position of cortical segments for cell type counts, we measured the cortical ventricle from the corticostriatal boundary to the apex, defined the 50% position, and centered at this position a 200-μm-wide box perpendicular to the ventricle. All imaging was carried out on a Nikon A1 laser scanning confocal microscope.

Lamination assay

P0 or P7 brains were fixed and sectioned as described for "Morphological Analysis" above. Slides were incubated for 24 h at 4 °C in a blocking solution containing normal donkey serum (5% v/v) diluted in PBS-T (1× phosphate buffered saline and 0.01% (v/v) Triton X-100), rinsed in PBS-T, and incubated for 24 h at 4°C in primary antibody solution containing anti-Ctip2[44] (ab18465; Abcam), anti-Tbr1[44] (ab31940; Abcam) and anti-Brn2[45] (sc-6029; Santa Cruz Biotechnology) antibodies, each diluted 1:500 in PBS-T. These antibodies have been previously used for IHC analysis in brain[46,47]. The slides were then rinsed in PBS-T and incubated overnight at 4°C in fluorophore-conjugated secondary antibodies (711-545-152 and 712-165-153; Jackson ImmunoResearch). Slides were rinsed in PBS-T, counterstained for 2 h in DAPI (D1306, Thermo-Fisher), rinsed in PBS-T and coverslip-mounted with Fluoromount-G (SouthernBiotech). Sections were imaged on a Nikon Eclipse E600 upright microscope with a 4× objective lens (Plan Apo; N.A. 0.2), mercury light source, appropriate fluorescent filter sets, and NIS Elements software, (v. 4.20; Nikon Instruments). Images were imported into FIJI ImageJ (v. 1.50E[48]) and similar

sections from each brain were identified based on anatomical landmarks. Within each genotype, all brains were selected randomly for histological processing without taking morphological criteria into account. All histology was done blind, by investigators that were unaware of group allocation. No data points were excluded. Male and female samples were used. All antibodies used for this study were validated and their use widely reported.

Behavioral testing

Subject mice were housed in a temperature-controlled vivarium maintained on a 12 h light-dark cycle. All procedures were approved by the University of California Davis Institutional Animal Care and Use Committee, and were conducted in accordance with the National Institutes of Health Guide for the Care and Use of Laboratory Animals. Efforts were made to minimize pain and distress and the number of animals used. No previous analyses were performed on animals used for behavioral testing. We used mixed genotype home cages with 2-4 animals per cage and used experimenters and video scorer/processors blinded to genotype during testing and analysis. All tests were conducted during the light cycle.

Chd8$^{+/del5}$ male and female mice and WT littermates, ages 2-4 months, were evaluated in a standard battery of neurobehavioral assays relevant to the core diagnostic and associated symptoms of ASD[16]. We performed the testing on two independent cohorts of adult *Chd8*$^{+/del5}$ mice (first cohort: 9 male, 10 female; second cohort: 11 male, 11 female) and WT littermates (first cohort: 11 male, 10 female; second cohort: 11 male, 9 female). One animal in the first cohort died during behavioral testing. This happened during the three-chambered social approach, in the middle of the behavioral battery. Adult *Chd8*$^{+/del5}$ and matched WT littermates were tested in the following sequence: open field, general health, self-grooming, marble burying, three-chambered social approach, male-female social interactions, novel object recognition, and fear conditioning. Testing was performed at the UC Davis MIND Institute Intellectual and Developmental Disabilities Research Center Mouse Behavior Core.

Open field locomotion—General exploratory locomotion in a novel open field environment was assayed as previously described[49-51]. Open field activity was considered an essential control for effects on physical activity, for example, sedation or hyperactivity[17,51,52], which could confound the interpretation of results from the reciprocal interactions, self-grooming, fear conditioning and social approach tasks. The testing room was illuminated at ~40 lx.

Adult general health and neurological reflexes—General health and neurological reflexes were evaluated in adult mice as previously described[53,54]. General health was assessed on a ranking scale of 0-3 based on fur condition, whisker condition, skin color, and body and limb tone. Body weight and basal temperature were also measured, using a hand held portable scale (Ohaus, Parsippany, NJ) and a mouse thermistor probe with lubricant and gently inserted 2 cm into the rectum, respectively. Righting reflex and any occurrences of physical abnormalities were noted. Neurological reflex tests included trunk curl, wire hanging, forepaw reaching, righting reflex, corneal reflex, whisker twitch, pinnae response, eyeblink response, and auditory startle. The reactivity level of each mouse was assessed with

tests measuring responsiveness to petting, intensity of a dowel biting response and level of vocalization during handling[55].

Novel object recognition—The novel object recognition test was conducted in opaque matte white (P95 White, Tap Plastics, Sacramento, CA) open field arenas (40 cm x 60 cm x 23 cm), using methods similar to those previously described[50,56]. The experiment consisted of three sessions: a 30-min exposure to the open field arena, a 10-min familiarization session and a 5-min recognition test. On day 1, each subject was habituated to a clean empty open field arena for 30 min. Twenty-four hours later, each subject was returned to the open field arena for 10 min for the habituation phase. The mouse was then removed from the open field and placed in a clean temporary holding cage for approximately 2 min. Two identical objects were placed in the arena. Each subject was returned to the open field in which it had been habituated and allowed to freely explore for 10 min. After the familiarization session, subjects were returned to their holding cages, which were transferred from the testing room to a nearby holding area. The open field was cleaned with 70% ethanol and let dry. One clean familiar object and one clean novel object were placed in the arena, where the two identical objects had been located during in the familiarization phase. Sixty minutes after the end of the familiarization session, each subject was returned to its open field for a 5 min recognition test, during which time it was allowed to freely explore the familiar object and the novel object. The familiarization session and the recognition test were videotaped and scored with Ethovision XT videotracking software (Version 9.0, Noldus Information Technologies, Leesburg, VA). Object investigation was defined as time spent sniffing the object when the nose was oriented toward the object and the nose-object distance was 2 cm or less. Recognition memory was defined as spending substantially more time sniffing the novel object than the familiar object. Total time spent sniffing both objects was used as a measure of general exploration. Time spent sniffing two identical objects during the familiarization phase confirmed the lack of an innate side bias. Objects used were plastic toys: a small soft plastic orange safety cone and a hard plastic magnetic cone with ribbed sides.

Repetitive self-grooming—Spontaneous repetitive self-grooming behavior was scored as previously described[17,49]. Each mouse was placed individually into a standard mouse cage, (46 cm long × 23.5 cm wide × 20 cm high). Cages were empty to eliminate digging in the bedding, which is a potentially competing behavior. The room was illuminated at ~40 lx. A front-mounted CCTV camera (Security Cameras Direct) was placed at ~1 m from the cages to record the sessions. Sessions were videotaped for 20 min. The first 10-min period was habituation and was unscored. Each subject was scored for cumulative time spent grooming all the body regions during the second 10 min of the test session.

Repetitive marble burying—Marble burying and digging in the bedding to cover the marbles was measured as previously described[49,57-59]. Twenty black glass marbles (15 mm in diameter) were arranged in a symmetrical 4 × 5-cm grid on top of 2-3 cm deep bedding in a clean standard mouse cage (27 × 16.5 × 12.5 cm) with a filter top lid. Each mouse was placed in the center of the cage for a 30-min exploration period, after which the number of

marbles buried was tallied by the investigator. 'Buried' was defined as greater than 50% covered by bedding[59]. Testing was performed under dim light (~15 lx).

Social approach—Social approach was tested in an automated three-chambered apparatus using methods similar to those previously described[49,60]. Automated Ethovision XT videotracking software (Version 9.0, Noldus Information Technologies, Leesburg, VA) and modified nonreflective materials for the chambers were employed to maximize throughput. The updated apparatus (40 cm × 60 cm × 23 cm) was a rectangular, three-chambered box made from matte white finished acrylic (P95 White, Tap Plastics, Sacramento, CA). Opaque retractable doors (12 cm × 33 cm) were designed to create optimal entryways between chambers (5 cm × 10 cm), while providing maximal manual division of compartments. Three zones, defined using the EthoVision XT software, detected time in each chamber for each phase of the assay. Zones were defined as the annulus extending 2 cm from each novel object or novel mouse enclosure (inverted wire cup, Galaxy Cup, Kitchen Plus, https://www.spectrumdiversified.com/whs/products/Galaxy-Pencil-Utility-Cup). Direction of the head, facing toward the cup enclosure, defined sniff time. A top-mounted infrared sensitive camera (Ikegami ICD-49, B&H Photo, New York, NY) was positioned directly above every pair of three-chambered units. Infrared lighting (Nightvisionexperts.com) provided uniform, low-level illumination. The subject mouse was first contained in the center chamber for 10 min, then allowed to explore all three empty chambers during a 10-min habituation session, then allowed to explore the three chambers containing a novel object in one side chamber and a novel mouse in the other side chamber. Lack of innate side preference was confirmed during the initial 10 min of habituation to the entire arena. Novel stimulus mice were 129Sv/ImJ, a relatively inactive strain, aged 10–14 weeks, and matched to the subject mice by sex. Number of entries into the side chambers served as a within-task control for levels of general exploratory locomotion.

Male-female social interaction—The male-female reciprocal social interaction test was conducted as previously described[49,61]. Briefly, each freely moving male subject was paired for 5-min with a freely moving unfamiliar estrous WT female. A closed-circuit television camera (Panasonic, Secaucus, NJ, USA) was positioned at an angle from the Noldus PhenoTyper arena (Noldus, Leesburg, VA) for optimal video quality. An ultrasonic microphone (Avisoft UltraSoundGate condenser microphone capsule CM15; Avisoft Bioacoustics, Berlin, Germany) was mounted 20 cm above the cage. Sampling frequency for the microphone was 250 kHz, and the resolution was 16 bits. The entire apparatus was contained in a sound-attenuating environmental chamber (Lafayette Instruments, Lafayette, IN) under dim LED illumination (~10 lx). Duration of nose-to-nose sniffing, nose-to-anogenital sniffing, and following were scored using Noldus Observer 8.0XT event recording software (Noldus, Leesburg, VA) as previously described[49]. Ultrasonic vocalization spectrograms were displayed using Avisoft software and calls were identified manually by a highly trained investigator blinded to genotype.

Fear conditioning—Delay contextual and cued fear conditioning was conducted using an automated fear-conditioning chamber (Med Associates, St Albans, VT, USA) as previously described[62]. The conditioning chamber (32 × 25 × 23 cm3, Med Associates) interfaced with

a PC installed with VideoFreeze software (version 1.12.0.0, Med Associates) and enclosed in a sound-attenuating cubicle. Training consisted of a 2-min acclimation period followed by three tone-shock (CS–US) pairings (80 dB tone, duration 30 s; 0.5 mA footshock, duration 1 s; intershock interval 90 s) and a 2.5-min period, during which no stimuli were presented. The environment was well lit (~100 lx), with a stainless steel grid floor and swabbed with vanilla odor cue (prepared from vanilla extract; McCormick; 1:100 dilution). A 5-min test of contextual fear conditioning was performed 24 h after training, in the absence of the tone and footshock but in the presence of 100 lx overhead lighting, vanilla odor and chamber cues identical to those used on the training day. Cued fear conditioning, conducted 48 h after training, was assessed in a novel environment with distinct visual, tactile and olfactory cues. Overhead lighting was turned off. The cued test consisted of a 3-min acclimation period followed by a 3-min presentation of the tone CS and a 90-s exploration period. Cumulative time spent freezing in each condition was quantified by VideoFreeze software (Med Associates).

MRI within brains of the subjects assessed in behavioral assays

Perfusion—Mice from the first cohort (*Chd8*$^{+/del5}$: 9 male, 10 female; WT: 8 male, 10 female) that had undergone the behavioral assays were anesthetized with isoflurane (4% to effect) and intracardially perfused with 30 mL of 0.1 M PBS containing 10 U/mL heparin (Sigma) and 2 mM ProHance (a Gadolinium contrast agent) followed by 30 mL of 4% paraformaldehyde (PFA) containing 2 mM ProHance[63,64]. Mice were perfused, and then decapitated and the skin, lower jaw, ears, and the cartilaginous nose tip were removed. The brain and remaining skull structures were incubated in 4% PFA + 2 mM ProHance overnight at 4 °C then transferred to 0.1 M PBS containing 2 mM ProHance and 0.02% sodium azide for at least 7 d before MRI scanning.

After perfusion, a multichannel 7.0 Tesla MRI scanner (Agilent Inc., Palo Alto, CA) was used to image the brains within their skulls. Sixteen custom-built solenoid coils were used to image the brains in parallel[65]. In order to detect volumetric changes via anatomical imaging, we used the following parameters for the anatomical MRI scans: T2-weighted, 3-D fast spin-echo sequence, with a cylindrical acquisition of k-space[66], a TR of 350 ms and TEs of 12 ms per echo for 6 echoes, field-of-view equal to 20 × 20 × 25 mm^3 and matrix size equal to 504 × 504 × 630 mm^3. Our parameters output an image with 0.040 mm isotropic voxels. The total imaging time was 14 h.

Diffusion tensor imaging

Diffusion tensor imaging (DTI) was done using a 3D diffusion weighted fast spin echo sequence (FSE), with an echo train length of 6. Parameters for the DTI sequence were: TR = 270 ms, first TE = 30 ms, and TEs of 10 ms for the remaining five echoes, 1 average. We used a field-of-view m(FOV) of 14 × 14 × 25 mm^3 and a matrix size of 180 × 180 × 324 mm^3, yielding an image with 0.078-mm isotropic voxels. We acquired five b = 0 s/mm^2 images and 30 high b-value (b = 2,147 s/mm^2) images in 30 different directions, using the Jones30 scheme[67]. Total imaging time was ~12 h. After acquisition, the images were analyzed using the FSL software package (FMRIB, Oxford UK), which was used to create

fractional anisotropy (FA), mean diffusivity (MD), axial diffusivity (AD) and radial diffusivity (RD) maps for each of the brains used in this study.

Structural MRI registration and analysis

To visualize and compare any changes in the mouse brains the images (or b = 0 s/mm^2 images for DTI) are linearly (6 followed by 12 parameter) and nonlinearly registered together[68]. Registrations were performed with a combination of mni_autoreg tools[71] and ANTS (advanced normalization tools)[70,71]. All scans were then resampled with the appropriate transform and averaged to create a population atlas representing the average anatomy of the study sample. Note that the 40 μm anatomical images and the b = 0 s/mm^2 DTI images were registered separately. The result of the registration was to deform all images into alignment with each other in an unbiased fashion. For the volume measurements, this allowed us to analyze the deformations needed to take each individual mouse's anatomy into this final atlas space, the goal being to model how the deformation fields relate to genotype[72,73]. The Jacobian determinants of the deformation fields were then calculated as measures of volume at each voxel. For the diffusion measurements, the registration allowed us to analyze the intensity differences of all measures (FA, MD, AD, and RD) between genotypes. Significant volume changes and intensity differences could then be calculated by warping a pre-existing classified MRI atlas onto the population atlas, which allowed us to assess the volume or mean diffusion measure (FA, MD, AD and RD) of 159 different segmented structures encompassing cortical lobes, large white matter structures (i.e., corpus callosum), ventricles, cerebellum, brain stem and olfactory bulbs[68,74,75], in all brains. Further, these measurements could be examined on a voxelwise basis to localize the differences found within regions or across the brain. Multiple comparisons in this study were controlled for using the false discovery rate[76]. We reported combined sex results in the main text.

Genomics

Bulk forebrains were microdissected from *Chd8*$^{+/del5}$ and matched WT littermates at e12.5, e14.5, e17.5, P0 and from adults (represented in plots as >P56). Dissection included whole forebrain hemispheres after removing surface tissue and skull for all ages except e12.5, when the anterior portion of the developing head was collected. Dissections were performed blind to genotype. Samples included males and females of each genotype at each stage; exact numbers are reported in Table S2. Total RNA was isolated using Ambion RNAqueous and assayed using an Agilent BioAnalyzer instrument. Stranded mRNA sequencing libraries were prepared using TruSeq Stranded mRNA kits; 6-12 samples per lane were pooled and sequenced on the Illumina HiSeq platform using a single-end 50-bp (e14.5, e17.5, P0 and adult) or paired-end 100-bp (e12.5) strategy. Each library was quantified and pooled before submission for sequencing. e12.5 samples were sequenced at the UC Berkeley Genomics Sequencing Laboratory; all other samples were sequenced at the UC Davis DNA Technologies Core. Reads from RNA-seq were aligned to the mouse genome (mm9) using STAR (version 2.4.2a)[77]. Aligned reads mapping to genes were counted at the gene level using subread featureCounts[78]. The mm9 knownGene annotation track and aligned reads were used to generate quality control information using the full RSeQC tool suite[79]. Samples that exhibited strong 3' bias using geneBody_coverage.py or poor exon distribution

using read_distribution.py were discarded. Unaligned reads were quality checked by FastQC. BLAST[80] was used to identify reads that mapped to either the reference or 5-bp and 14-bp deletions at *Chd8* exon 5to verify genotype and test for deletion allele transcript frequency.We performed quantitative reverse transcription PCR to validate DE and DS analysis using cDNA libraries prepared using the same protocols, with primers reported in Table S4. Cycle counts were normalized to *ActB* and compared via standard methods as discussed in the methods.

Differential expression analysis and permutation testing

Raw count data for all samples were used as input along with sample information for differential expression analysis using edgeR[81]. Genes with at least 10 reads per million in at least two individual samples were included for analysis, resulting in a final set of 11,936 genes for differential testing. Multidimensional scaling analysis indicated that the strongest driver of variance across samples was developmental stage, with no obvious separation between wild-type and $Chd8^{+/del5}$ samples. Tagwise dispersion estimates were generated and differential expression analysis was performed with edgeR[81] using a generalized linear model including sex, developmental stage, and sequencing run factor-based covariates and using genotype as the variable for testing. Stage-specific differential expression testing was also performed. Normalized expression levels were generated using the egdeR rpkm function followed by removing the sequencing batch effect via the limma removeBatchEffect function. Normalized log2(RPKM) values were used for plotting of summary heatmaps and of expression data for individual genes. We examined DE results obtained with reduced coverage criteria for gene inclusion, which resulted in identification of DE genes with lower CPM but no major differences in overall findings. Permutation testing was performed by testing for set inclusion between differentially down- or upregulated genes identified in the full model and annotated gene sets, comparing observed with expected overlap. Observed overlap was calculated as the overlapping genes, whereas the expected overlap distribution was generated via iterative random sampling of the same number of genes as in the annotated gene set, followed by testing for overlap of randomly selected genes with DE genes. Random sampling was repeated 100,000 times, enabling us to estimate the mean and standard derivation of the expected distribution. Based on this distribution, empirical z-score and p-values were calculated for the observed overlap. All analysis was performed in R using custom scripts which are available upon request.

ChIP-seq analysis

Adult mouse forebrain was dissected on ice, cross-linked using formaldehyde and lysed with SDS, and the DNA was sonicated on a Covaris instrument using standard ChIP-seq protocols adapted for mouse tissues[82]. Chromatin immunoprecipitation (ChIP) was performed using antibodies for Chd8 (ab114126; Abcam). This antibody has been used for brain or neuronal Chd8 ChIP-seq in a previous publication[12]. DNA libraries of matched input and ChIP samples were prepared using the Nugen Ovation Ultralow Library System V2, indexed for multiplexed runs of four libraries per lane, and sequenced on an Illumina HiSeq 4000 instrument using a single-end 50-bp strategy. Resulting reads were filtered to remove artifacts and low quality sequences and then mapped to the mouse genome (mm9) using the BWA algorithm[83].

BWA call: bwa aln – t 6 – l 25 mm9 sample.fastq.gz

We used MACS[84] to identify significant peaks, disabling model-based peak identification and local significance testing. Peaks were called for each individual ChIP-seq experiment versus matched input control, as well as for merged ChIP and control data using MACS1.4.

MACS call: macs14 – t chip.bam – – control=input.bam – name = chip_output – –
format = BAM – – gsize = mm – – tsize = 50 – – bw = 300 – – mfold = 10, 30 – – nolambda –
– nomodel –
– shiftsize = 150 – p 0.0001

After peak calling, enriched regions were filtered to remove ENCODE blacklist regions and annotated using custom scripts. As nearly all peaks were at gene promoters, functional annotation was performed on the promoter-bound gene sets using ENRICHR[85]. We performed de novo motif discovery using RSAT using default parameters[86]. We additionally analyzed available Chd8 ChIP-seq data[11-13]. For comparison, all datasets were run through the same analysis pipeline and are available as UCSC TrackHubs for upload to the UCSC Genome Browser.

WGCNA

We used the WGCNA package[25] in R (version 3.2.3) to construct signed co-expression networks using any gene expressed at an RPKM value of 0.25 or higher in at least one sample. A correlation matrix using the biweight midcorrelation between all genes was computed for all relevant samples. The soft thresholding power was estimated and used to derive an adjacency matrix exhibiting approximate scale-free topology ($R^2 > 0.85$). The adjacency matrix was transformed to a topological overlap matrix (TOM). The matrix 1-TOM was used as the input to calculate co-expression modules using hierarchical clustering. Modules were branches of the hierarchical cluster tree base, using the cutreeHybrid function in WGCNA[87], with minimum module size set to 500 genes. Genes with positively correlated expression and high topological overlap were clustered together in these modules. In addition, Pearson's correlation coefficients were used to calculate correlation between sample traits (for example, genotype) and modules. The expression profile of a given module was summarized by the module eigengene, ME. Modules with highly correlated MEs (correlation > 0.80) were merged together. The module connectivity (kME) of each gene was calculated by correlating the gene expression profile with module eigengenes. Four modules were generated using this method and were reordered in descending order by gene set size and named numerically. Genes with no network correlation were placed into the module M.grey. We repeated module generation using only wild-type samples, only *Chd8*$^{+/del5}$ samples, and with/without adult samplesm with largely the same results as for the full sample set, which is consistent with the finding that most DE gene expression changes are far smaller than changes for genes across developmental stages.

Gene Ontology enrichment and protein-protein interaction network analysis

Permutation testing was performed to test for overlap between DE genes and published gene sets. Human Gene Ontology (GO) data was downloaded from Bioconductor (org.Hs.egGO2ALLEGS, org.Hs.eg.db, GO.db). We used the TopGO[88] program to test for enrichment of GO terms indicating parent:child relationships. For the analysis presented here, we restricted our testing to GO Biological Process annotations and required a minimal node size (number of genes annotated to GO terms) of 20. We used the internal 'weight01' testing framework and the Fisher test, a strategy recommended for gene set analysis that generally accounts for multiple testing comparisons. For GO analysis, we examined down- and upregulated genes separately, repeating the analysis on DE genes from the full model (cutoff of FDR < 0.20) for all genes and by expression module and stage-specific genes sets (cutoff of $p < 0.05$). For all enrichment analysis, the test set of DE genes was compared against the background set of genes expressed in our study based on minimum read count cutoffs described above. Genes with expected/observed ratios of at least 1.5 fold were considered enriched. Heatmaps showing positive log2(expected/observed) values were plotted for GO terms of interest. Protein-protein interaction enrichment and network generation for module-specific DE gene sets was performed using STRING[27], considering only experimentally-defined and database interactions. Only module M.1 exhibited a significant enrichment in protein-protein interactions. We compared TopGO enrichment results with goseq[89], correcting for gene length, and compared STRING proteinprotein interaction with DAPPLE[90], with no substantial differences observed for either methods comparison.

MISO analysis

The Mixture-of-Isoforms (MISO) statistical model[30] was used to identify alternative transcript events in our RNA-seq data. For MISO analysis, individual aligned bam files were sorted and merged based on genotype and developmental stage (for example, e17.5 WT and e17.5 *Chd8*$^{+/del5}$). One sample (S159) from the e17.5 *Chd8*$^{+/del5}$ group was discarded from analysis because the sample had lower read coverage compared to the other samples, and was significantly impacting MISO results across genotype. Analysis was performed using the standard MISO software package *fastmiso* (https://github.com/yarden/MISO). Standard GFF alternate event annotations for mm9 (version 1) were used. MISO was run to compute PSI scores (miso –run) using standard, unfiltered parameters. Comparisons (compare_miso) were run between either genotype for a specific stage (for example, e17.5 *Chd8*$^{+/del5}$ versus e17.5 WT) or pairwise between WT stages (for example, e14.5 WT versus e17.5 WT). Results were filtered (filter_events) based on the following parameters: --num-total=100, --num-sum-inc-exc=10, --delta-psi=0.1, --bayes-factor=100.

Statistical analysis

General—No statistical methods were used to predetermine sample sizes with the exception of behavioral studies, but other sample sizes are similar to those reported in previous publications[12,13]. Data collection and analysis were not performed blind to the conditions of the experiments for ChIP-seq, western blots or qRT-PCR. All other data collection and analyses were performed blind. Data collection was randomized across litters

for RNA-seq, western blots and histology assays. Aside from behavioral analyses, data distribution was assumed to be normal and not formally tested.

Neuroanatomy, biochemistry, and immunostaining—All statistical analyses and plots were generated using GraphPad Prism 7.0a. Two-tailed t-tests were used for all analyses comparing two groups. For comparisons of three or more data sets, one-way ANOVA followed by post-hoc two-tailed t-tests were used. A minimum of three biological replicates (individual animals) were used for all genotypes and assays. For isoform-specific qPCR, comparisons across stage and genotype were analyzed using two-tailed Welch's t-test and linear regression.

Behavior—Data were analyzed with Statistica software (Tulsa, OK, USA). Plots were generated using GraphPad Prism 7.0a. Sexes were considered separately with genotype as the fixed factor. Statistical testing was performed using established assay-specific methods, including Student's t-test for single parameter comparisons between genotypes, and one-way or two-way repeated-measures ANOVA for comparisons across time points and/or between sexes. All significance levels were set at $p < 0.05$ and all t-tests were two-tailed. Groups sizes indicated were chosen based on past experience and power analyses. Effects of genotype and sex were evaluated using multifactor ANOVA, as previously published[16,49,50,59,62]. Significant ANOVAs were followed by Tukey's honest significance difference (HSD) test. Behavioral analysis passed distribution normality tests, was collected using continuous variables and thus analyzed via parametric analysis, in all assays. For all behavioral analyses, variances were similar between groups and all data points within 2 s.d. of the mean were included in analysis.

Genomic analyses—Samples for RNA-seq were randomly collected across litters and processed blind to genotype. Samples from RNA-seq were removed if they failed to pass quality scoring and coverage criteria. For differential gene expression analysis, differences were considered statistically significant if FDR and p-values calculated by edgeR were < 0.20 and < 0.05, respectively. For permutation testing, For ChIP-seq, peaks were considered significant if p-values determined by MACS were < 0.0001. For permutation testing, enrichment was considered significant if empirical z-scores and p-values were > 2 and < 0.05, respectively. For differential splicing analysis, individual events were considered significant if the Bayes factor > 100 as calculated by MISO[30].

Data availability

The data that support the findings of this study are available from the corresponding author. DOIs for all published gene sets used in enrichment analysis: Sanders et al. 2015[19] -10.1016/j.neuron.2015.09.016; Parikshak et al. 2013[26] - 10.1016/j.cell.2013.10.031; Cotney et al. 2015[12] - 10.1038/ncomms7404; Willsey et al. 2015[21] - 10.1016/j.cell.2013.10.020; Sugathan et al. 2014[11] - 10.1073/pnas.1405266111; Darnell et al. 2011[22] - 10.1016/j.cell.2011.06.013; Hormozdiari et al. 2014[20] - 10.1101/gr.178855.114; Katayama et al. 2016[13] -10.1038/nature19357; Durak et al. 2016[15] - 10.1038/nn.4400; and Parikshak et al. 2016[24] -10.1038/nature20612.

Code availability

All custom scripts and TrackHubs used for data processing and analysis are available at the Nord Lab Git Repository (https://github.com/NordNeurogenomicsLab/). A custom sample processing pipeline was used to align raw sequencing samples to mouse genome mm9 using RNA-seq aligner STAR (version 2.4.2a), features assigned via subreads featureCounts (version 1.5.0) to UCSC mm9 genes.gtf, and quality checks performed on individual samples using RSeQC (version 2.6.3). Differential expression analysis was done with a custom pipeline in R Studio using functions from edgeR (version 3.10.5) and limma (version 3.24.15). Permutation testing was performed with a custom R script. Co-expression network analysis was performed with a custom pipeline following the standard WGCNA (version 3.2.3) workflow and functions. Gene Ontology analysis was performed with a custom wrapper using standard the TopGO (version 2.20.0) program. ChIP-seq data was aligned to mm9 via BWA (version 0.6.2) and peaks were called via MACS (version 1.4.2). Peaks were then filtered to remove ENCODE blacklist regions and annotated. Comparison of enriched gene sets between RNA and ChIP-seq was performed using Enrichr (http://amp.pharm.mssm.edu/Enrichr/). MISO analysis (https://github.com/yarden/MISO/) was performed using standard parameters. See methods above for description and parameters.

Accession codes

Raw, aligned, and gene count data for RNA-seq and raw, aligned, and peak call data for ChIP-seq are available on GEO (Accession Number GSE99331).

Supplementary Material

Refer to Web version on PubMed Central for supplementary material.

Acknowledgments

Sequencing was performed at the UC Berkeley and UC Davis DNA cores. This work was supported by institutional funds from the UC Davis Center for Neuroscience, by the UC Davis MIND Institute Intellectual and Developmental Disabilities Research Center (U54 HD079125) and by NIGMS R35 GM119831. L.S.-F. was supported by the UC Davis Floyd and Mary Schwall Fellowship in Medical Research and by grant number T32-GM008799 from NIGMS-NIH. A.A.W. was supported by Training Grant number T32-GM007377 from NIH-NIGMS. R.C.-P. was supported by a Science Without Borders Fellowship from CNPq (Brazil). A.V., L.A.P. and D.E.D. were supported by National Institutes of Health grants R24HL123879, U01DE024427, R01HG003988, U54HG006997 and UM1HL098166. Research conducted at the E.O. Lawrence Berkeley National Laboratory was performed under Department of Energy Contract DE-AC02-05CH11231, University of California. J.E. and J.P.L. were supported by the Canadian Institute for Health Research, Brain Canada and the Ontario Brain Institute.

References

1. Ho L, Crabtree GR. Chromatin remodelling during development. Nature. 2010; 463:474–484. [PubMed: 20110991]
2. Chen T, Dent SYR. Chromatin modifiers and remodellers: regulators of cellular differentiation. Nat Rev Genet. 2014; 15:93–106. [PubMed: 24366184]
3. Ronan JL, Wu W, Crabtree GR. From neural development to cognition: unexpected roles for chromatin. Nat Rev Genet. 2013; 14:347–359. [PubMed: 23568486]
4. Sanders SJ. First glimpses of the neurobiology of autism spectrum disorder. Curr Opin Genet Dev. 2015; 33:80–92. [PubMed: 26547130]

5. McCarthy SE, et al. De novo mutations in schizophrenia implicate chromatin remodeling and support a genetic overlap with autism and intellectual disability. Mol Psychiatry. 2014; 19:652–658. [PubMed: 24776741]
6. Vissers LELM, Gilissen C, Veltman JA. Genetic studies in intellectual disability and related disorders. Nat Rev Genet. 2016; 17:9–18. [PubMed: 26503795]
7. De Rubeis S, et al. Synaptic, transcriptional and chromatin genes disrupted in autism. Nature. 2014; 515:209–215. [PubMed: 25363760]
8. Iossifov I, et al. The contribution of *de novo* coding mutations to autism spectrum disorder. Nature. 2014; 515:216–221. [PubMed: 25363768]
9. Bernier R, et al. Disruptive *CHD8* mutations define a subtype of autism early in development. Cell. 2014; 158:263–276. [PubMed: 24998929]
10. Nishiyama M, et al. Early embryonic death in mice lacking the beta-catenin-binding protein Duplin. Mol Cell Biol. 2004; 24:8386–8394. [PubMed: 15367660]
11. Sugathan A, et al. CHD8 regulates neurodevelopmental pathways associated with autism spectrum disorder in neural progenitors. Proc Natl Acad Sci USA. 2014; 111:E4468–E4477. [PubMed: 25294932]
12. Cotney J, et al. The autism-associated chromatin modifier CHD8 regulates other autism risk genes during human neurodevelopment. Nat Commun. 2015; 6:6404. [PubMed: 25752243]
13. Katayama Y, et al. CHD8 haploinsufficiency results in autistic-like phenotypes in mice. Nature. 2016; 537:675–679. [PubMed: 27602517]
14. Platt RJ, et al. Chd8 Mutation Leads to autistic-like behaviors and impaired striatal circuits. Cell Reports. 2017; 19:335–350. [PubMed: 28402856]
15. Durak O, et al. Chd8 mediates cortical neurogenesis via transcriptional regulation of cell cycle and Wnt signaling. Nat Neurosci. 2016; 19:1477–1488. [PubMed: 27694995]
16. Silverman JL, Yang M, Lord C, Crawley JN. Behavioural phenotyping assays for mouse models of autism. Nat Rev Neurosci. 2010; 11:490–502. [PubMed: 20559336]
17. Silverman JL, Babineau BA, Oliver CF, Karras MN, Crawley JN. Influence of stimulant-induced hyperactivity on social approach in the BTBR mouse model of autism. Neuropharmacology. 2013; 68:210–222. [PubMed: 22968082]
18. Croft D, et al. The Reactome pathway knowledgebase. Nucleic Acids Res. 2014; 42:D472–D477. [PubMed: 24243840]
19. Sanders SJ, et al. Insights into autism spectrum disorder genomic architecture and biology from 71 risk loci. Neuron. 2015; 87:1215–1233. [PubMed: 26402605]
20. Hormozdiari F, Penn O, Borenstein E, Eichler EE. The discovery of integrated gene networks for autism and related disorders. Genome Res. 2015; 25:142–154. [PubMed: 25378250]
21. Willsey AJ, et al. Coexpression networks implicate human midfetal deep cortical projection neurons in the pathogenesis of autism. Cell. 2013; 155:997–1007. [PubMed: 24267886]
22. Darnell JC, et al. FMRP stalls ribosomal translocation on mRNAs linked to synaptic function and autism. Cell. 2011; 146:247–261. [PubMed: 21784246]
23. Voineagu I, et al. Transcriptomic analysis of autistic brain reveals convergent molecular pathology. Nature. 2011; 474:380–384. [PubMed: 21614001]
24. Parikshak NN, et al. Genome-wide changes in lncRNA, splicing, and regional gene expression patterns in autism. Nature. 2016; 540:423–427. [PubMed: 27919067]
25. Langfelder P, Horvath S. WGCNA: an R package for weighted correlation network analysis. BMC Bioinformatics. 2008; 9:559. [PubMed: 19114008]
26. Parikshak NN, et al. Integrative functional genomic analyses implicate specific molecular pathways and circuits in autism. Cell. 2013; 155:1008–1021. [PubMed: 24267887]
27. Jensen LJ, et al. STRING 8–a global view on proteins and their functional interactions in 630 organisms. Nucleic Acids Res. 2009; 37:D412–D416. [PubMed: 18940858]
28. Alrahbeni T, et al. Full UPF3B function is critical for neuronal differentiation of neural stem cells. Mol Brain. 2015; 8:33. [PubMed: 26012578]

29. Laumonnier F, et al. Mutations of the *UPF3B* gene, which encodes a protein widely expressed in neurons, are associated with nonspecific mental retardation with or without autism. Mol Psychiatry. 2010; 15:767–776. [PubMed: 19238151]
30. Katz Y, Wang ET, Airoldi EM, Burge CB. Analysis and design of RNA sequencing experiments for identifying isoform regulation. Nat Methods. 2010; 7:1009–1015. [PubMed: 21057496]
31. Zhang X, et al. Cell-type-specific alternative splicing governs cell fate in the developing cerebral cortex. Cell. 2016; 166:1147–1162.e15. [PubMed: 27565344]
32. Tipps ME, Raybuck JD, Buck KJ, Lattal KM. Delay and trace fear conditioning in C57BL/6 and DBA/2 mice: issues of measurement and performance. Learn Mem. 2014; 21:380–393. [PubMed: 25031364]
33. Brunner D, et al. Comprehensive analysis of the 16p11.2 deletion and null Cntnap2 mouse models of autism spectrum disorder. PLoS One. 2015; 10:e0134572. [PubMed: 26273832]
34. Ellegood J, et al. Clustering autism: using neuroanatomical differences in 26 mouse models to gain insight into the heterogeneity. Mol Psychiatry. 2015; 20:118–125. [PubMed: 25199916]
35. Etherton MR, Blaiss CA, Powell CM, Südhof TC. Mouse neurexin-1alpha deletion causes correlated electrophysiological and behavioral changes consistent with cognitive impairments. Proc Natl Acad Sci USA. 2009; 106:17998–18003. [PubMed: 19822762]
36. Orosco LA, et al. Loss of Wdfy3 in mice alters cerebral cortical neurogenesis reflecting aspects of the autism pathology. Nat Commun. 2014; 5:4692. [PubMed: 25198012]
37. Hagerman R, Au J, Hagerman P. FMR1 premutation and full mutation molecular mechanisms related to autism. J Neurodev Disord. 2011; 3:211–224. [PubMed: 21617890]
38. Lee JA, et al. Cytoplasmic Rbfox1 regulates the expression of synaptic and autism-related genes. Neuron. 2016; 89:113–128. [PubMed: 26687839]
39. Mali P, et al. RNA-guided human genome engineering via Cas9. Science. 2013; 339:823–826. [PubMed: 23287722]
40. Du C, Ma X, Meruvu S, Hugendubler L, Mueller E. The adipogenic transcriptional cofactor ZNF638 interacts with splicing regulators and influences alternative splicing. J Lipid Res. 2014; 55:1886–1896. [PubMed: 25024404]
41. Yoo SW, Motari MG, Schnaar RL. Agenesis of the corpus callosum in Nogo receptor deficient mice. J Comp Neurol. 2017; 525:291–301. [PubMed: 27339102]
42. Yeung J, Ha TJ, Swanson DJ, Goldowitz D. A novel and multivalent role of Pax6 in cerebellar development. J Neurosci. 2016; 36:9057–9069. [PubMed: 27581449]
43. Nguyen KH, Yao XH, Erickson AG, Mishra S, Nyomba BLG. Glucose intolerance in aging male IGFBP-3 transgenic mice: differential effects of human IGFBP-3 and its mutant IGFBP-3 devoid of IGF binding ability. Endocrinology. 2015; 156:462–474. [PubMed: 25490144]
44. Galazo MJ, Emsley JG, Macklis JD. Corticothalamic projection neuron development beyond subtype specification: Fog2 and intersectional controls regulate intraclass neuronal diversity. Neuron. 2016; 91:90–106. [PubMed: 27321927]
45. Espuny-Camacho I, et al. Hallmarks of Alzheimer's disease in stem-cell-derived human neurons transplanted into mouse brain. Neuron. 2017; 93:1066–1081.e8. [PubMed: 28238547]
46. Huang Z, Yu Y, Shimoda Y, Watanabe K, Liu Y. Loss of neural recognition molecule NB-3 delays the normal projection and terminal branching of developing corticospinal tract axons in the mouse. J Comp Neurol. 2012; 520:1227–1245. [PubMed: 21935948]
47. Lloyd-Burton S, Roskams AJ. SPARC-like 1 (SC1) is a diversely expressed and developmentally regulated matricellular protein that does not compensate for the absence of SPARC in the CNS. J Comp Neurol. 2012; 520:2575–2590. [PubMed: 22173850]
48. Schindelin J, et al. Fiji: an open-source platform for biological-image analysis. Nat Methods. 2012; 9:676–682. [PubMed: 22743772]
49. Silverman JL, et al. GABAB receptor agonist R-baclofen reverses social deficits and reduces repetitive behavior in two mouse models of autism. Neuropsychopharmacology. 2015; 40:2228–2239. [PubMed: 25754761]
50. Flannery BM, et al. Behavioral assessment of NIH Swiss mice acutely intoxicated with tetramethylenedisulfotetramine. Neurotoxicol Teratol. 2015; 47:36–45. [PubMed: 25446016]

51. Silverman JL, et al. Negative allosteric modulation of the mGluR5 receptor reduces repetitive behaviors and rescues social deficits in mouse models of autism. Sci Transl Med. 2012; 4:131ra51–131ra51.
52. Silverman JL, et al. Low stress reactivity and neuroendocrine factors in the BTBR T+tf/J mouse model of autism. Neuroscience. 2010; 171:1197–1208. [PubMed: 20888890]
53. Wöhr M, Scattoni ML. Behavioural methods used in rodent models of autism spectrum disorders: current standards and new developments. Behav Brain Res. 2013; 251:5–17. [PubMed: 23769995]
54. Chadman KK, et al. Minimal aberrant behavioral phenotypes of neuroligin-3 R451C knockin mice. Autism Res. 2008; 1:147–158. [PubMed: 19360662]
55. Rogers DC, et al. Behavioral and functional analysis of mouse phenotype: SHIRPA, a proposed protocol for comprehensive phenotype assessment. Mamm Genome. 1997; 8:711–713. [PubMed: 9321461]
56. Yang M, Lewis FC, Sarvi MS, Foley GM, Crawley JN. 16p11.2 Deletion mice display cognitive deficits in touchscreen learning and novelty recognition tasks. Learn Mem. 2015; 22:622–632. [PubMed: 26572653]
57. Thomas AM, Bui N, Perkins JR, Yuva-Paylor LA, Paylor R. Group I metabotropic glutamate receptor antagonists alter select behaviors in a mouse model for fragile X syndrome. Psychopharmacology (Berl). 2012; 219:47–58. [PubMed: 21656124]
58. Thomas A, et al. Marble burying reflects a repetitive and perseverative behavior more than novelty-induced anxiety. Psychopharmacology (Berl). 2009; 204:361–373. [PubMed: 19189082]
59. Henderson C, et al. Reversal of disease-related pathologies in the fragile X mouse model by selective activation of GABAB receptors with arbaclofen. Sci Transl Med. 2012; 4:152ra128–152ra128.
60. Yang, M., Silverman, JL., Crawley, JN. Automated three-chambered social approach task for mice. In: Gerfen, CR.Holmes, A.Sibley, D.Skolnick, P., Wray, S., editors. Current Protocols in Neuroscience. Wiley; 2011. p. 26.8-26.16.Chapter 8, Unit 8
61. Scattoni ML, Ricceri L, Crawley JN. Unusual repertoire of vocalizations in adult BTBR T+tf/J mice during three types of social encounters. Genes Brain Behav. 2011; 10:44–56. [PubMed: 20618443]
62. Bales KL, et al. Long-term exposure to intranasal oxytocin in a mouse autism model. Transl Psychiatry. 2014; 4:e480. [PubMed: 25386957]
63. Skrzypiec-Spring M, Grotthus B, Szelag A, Schulz R. Isolated heart perfusion according to Langendorff—still viable in the new millennium. J Pharmacol Toxicol Methods. 2007; 55:113–126. [PubMed: 16844390]
64. Cahill LS, et al. Preparation of fixed mouse brains for MRI. Neuroimage. 2012; 60:933–939. [PubMed: 22305951]
65. Bock NA, et al. In vivo magnetic resonance imaging and semiautomated image analysis extend the brain phenotype for cdf/cdf mice. J Neurosci. 2006; 26:4455–4459. [PubMed: 16641223]
66. Nieman BJ, et al. Fast spin-echo for multiple mouse magnetic resonance phenotyping. Magn Reson Med. 2005; 54:532–537. [PubMed: 16086298]
67. Jones DK, Horsfield MA, Simmons A. Optimal strategies for measuring diffusion in anisotropic systems by magnetic resonance imaging. Magn Reson Med. 1999; 42:515–525. [PubMed: 10467296]
68. Dorr AE, Lerch JP, Spring S, Kabani N, Henkelman RM. High resolution three-dimensional brain atlas using an average magnetic resonance image of 40 adult C57Bl/6J mice. Neuroimage. 2008; 42:60–69. [PubMed: 18502665]
69. Collins DL, Neelin P, Peters TM, Evans AC. Automatic 3D intersubject registration of MR volumetric data in standardized Talairach space. J Comput Assist Tomogr. 1994; 18:192–205. [PubMed: 8126267]
70. Avants BB, et al. A reproducible evaluation of ANTs similarity metric performance in brain image registration. Neuroimage. 2011; 54:2033–2044. [PubMed: 20851191]
71. Avants BB, Epstein CL, Grossman M, Gee JC. Symmetric diffeomorphic image registration with cross-correlation: evaluating automated labeling of elderly and neurodegenerative brain. Med Image Anal. 2008; 12:26–41. [PubMed: 17659998]

72. Lerch JP, et al. Cortical thickness measured from MRI in the YAC128 mouse model of Huntington's disease. Neuroimage. 2008; 41:243–251. [PubMed: 18387826]
73. Nieman BJ, Flenniken AM, Adamson SL, Henkelman RM, Sled JG. Anatomical phenotyping in the brain and skull of a mutant mouse by magnetic resonance imaging and computed tomography. Physiol Genomics. 2006; 24:154–162. [PubMed: 16410543]
74. Steadman PE, et al. Genetic effects on cerebellar structure across mouse models of autism using a magnetic resonance imaging atlas. Autism Res. 2014; 7:124–137. [PubMed: 24151012]
75. Ullmann JFP, Janke AL, Reutens D, Watson C. Development of MRI-based atlases of non-human brains. J Comp Neurol. 2015; 523:391–405. [PubMed: 25236843]
76. Genovese CR, Lazar NA, Nichols T. Thresholding of statistical maps in functional neuroimaging using the false discovery rate. Neuroimage. 2002; 15:870–878. [PubMed: 11906227]
77. Dobin A, et al. STAR: ultrafast universal RNA-seq aligner. Bioinformatics. 2013; 29:15–21. [PubMed: 23104886]
78. Liao Y, Smyth GK, Shi W. featureCounts: an efficient general purpose program for assigning sequence reads to genomic features. Bioinformatics. 2014; 30:923–930. [PubMed: 24227677]
79. Wang L, Wang S, Li W. RSeQC: quality control of RNA-seq experiments. Bioinformatics. 2012; 28:2184–2185. [PubMed: 22743226]
80. Altschul SF, Gish W, Miller W, Myers EW, Lipman DJ. Basic local alignment search tool. J Mol Biol. 1990; 215:403–410. [PubMed: 2231712]
81. Robinson MD, McCarthy DJ, Smyth GK. edgeR: a Bioconductor package for differential expression analysis of digital gene expression data. Bioinformatics. 2010; 26:139–140. [PubMed: 19910308]
82. Nord AS, et al. Rapid and pervasive changes in genome-wide enhancer usage during mammalian development. Cell. 2013; 155:1521–1531. [PubMed: 24360275]
83. Li H, Durbin R. Fast and accurate short read alignment with Burrows-Wheeler transform. Bioinformatics. 2009; 25:1754–1760. [PubMed: 19451168]
84. Feng, J., Liu, T., Zhang, Y. Using MACS to identify peaks from ChIP-seq data. In: Bateman, A.Draghici, S.Khurana, E.Orchard, S., Pearson, WR., editors. Current Protocols in Bioinformatics. Wiley; 2011. p. 14Chapter 2, Unit 2
85. Chen EY, et al. Enrichr: interactive and collaborative HTML5 gene list enrichment analysis tool. BMC Bioinformatics. 2013; 14:128. [PubMed: 23586463]
86. Medina-Rivera A, et al. RSAT 2015: regulatory sequence analysis tools. Nucleic Acids Res. 2015; 43:W1, W50–6. [PubMed: 26136473]
87. Zhang B, Horvath S. A general framework for weighted gene co-expression network analysis. Stat Appl Genet Mol Biol. 2005; 4:e17.
88. Van Laere S, et al. Distinct molecular phenotype of inflammatory breast cancer compared to non-inflammatory breast cancer using Affymetrix-based genome-wide geneexpression analysis. Br J Cancer. 2007; 97:1165–1174. [PubMed: 17848951]
89. Young MD, Wakefield MJ, Smyth GK, Oshlack A. Gene ontology analysis for RNA-seq: accounting for selection bias. Genome Biol. 2010; 11:R14. [PubMed: 20132535]
90. Rossin EJ, et al. Proteins encoded in genomic regions associated with immune-mediated disease physically interact and suggest underlying biology. PLoS Genet. 2011; 7:e1001273. [PubMed: 21249183]

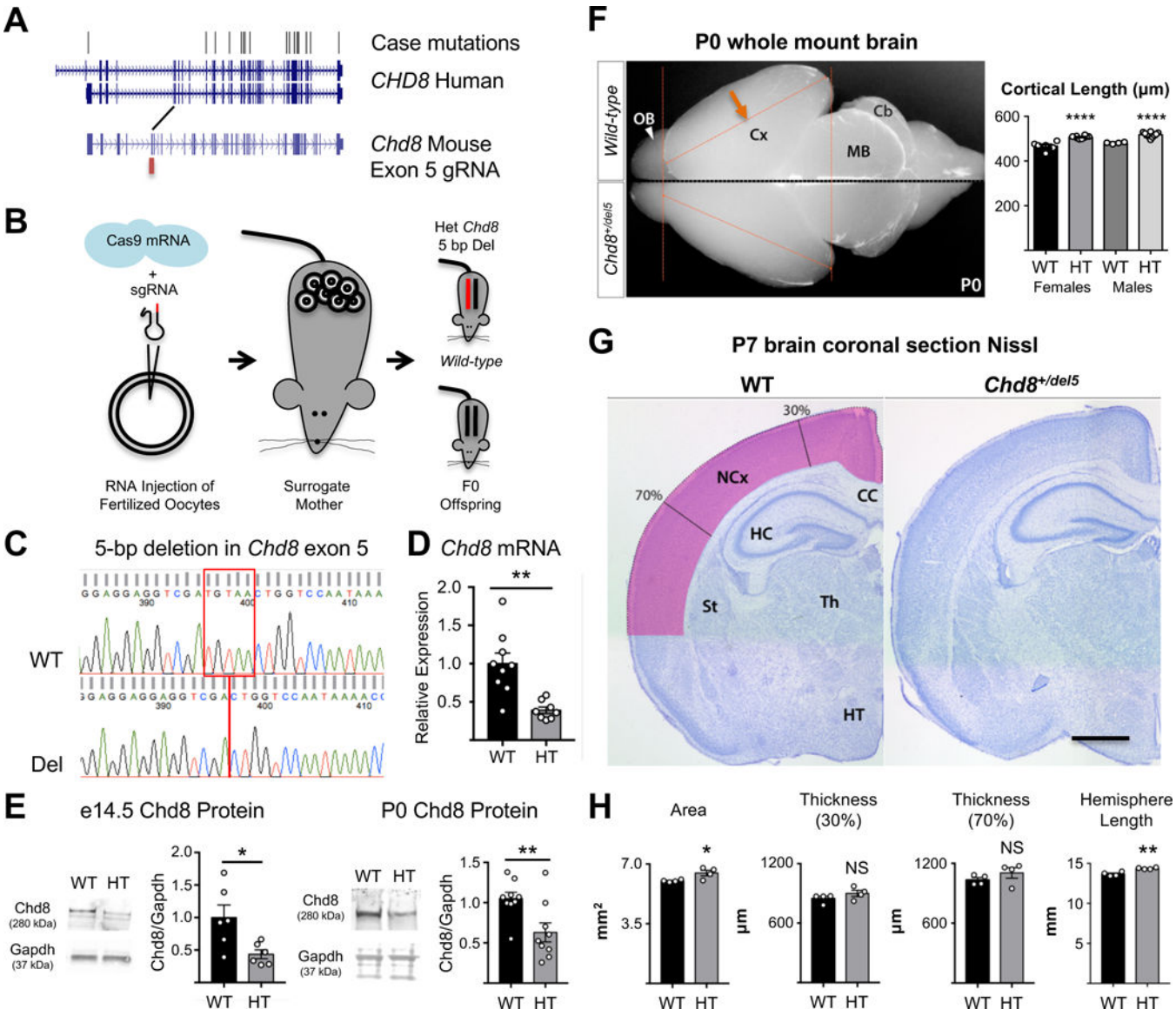

Figure 1. *Chd8*$^{+/del5}$ mouse model

A. Location of case mutations in human CHD8[9] (top) and corresponding guideRNA sequence homology for Cas9-targeting of mouse *Chd8* (bottom). **B.** Schematic of mouse line generation. Het, heterozygous; del, deletion. **C.** Sequence trace showing 5 bp deletion in exon 5. **D.** qRT-PCR showing reduction of RNA in *Chd8*$^{+/del5}$ (HT) forebrain at P0 (**p = 0.0076; n: WT = 9, *Chd8*$^{+/del5}$ = 8). E. Western blot of *Chd8*$^{+/del5}$ mice, showing reduction of Chd8 protein in *Chd8*$^{+/del5}$ forebrain at e14.5 (*p = 0.02; n: WT = 6, *Chd8*$^{+/del5}$ = 6) and P0 (**p = 0.0089; n: WT = 9, *Chd8*$^{+/del5}$ = 9). **F.** Whole-mount brain of *Chd8*$^{+/del5}$ mouse at P0 reveals increased cortical length (denoted by orange arrow and line), indicative of megalencephaly. OB: olfactory bulb, Cx: cortex, MB: midbrain, Cb: cerebellum. (****p < 0.0001; WT n: male = 4, female = 6; *Chd8*$^{+/del5}$ n: male = 10, female = 10). **G.** Representative coronal sections of WT and *Chd8*$^{+/del5}$ brains at P7 visualized with Nissl stain. Scale bar, 1 mm. Pink: measured neocortical area. NCx, neocortex; St, striatum; CC,

corpus callosum; HC, hippocampus; Th, thalamus; HTh, hypothalamus. **H.** Plots of cortical area, thickness at 30% and 70% distance from the dorsal midline, and cortical hemispheric circumference (dots representing individual samples; n = 4 mice each for both genotypes, *p: area = 0.0328, thickness (30%) = 0.224, thickness (70%) = 0.268, length **p = 0.0026). P-values derived using Student's t-test for D, E and H, and using one-way ANOVA for F. Error bars represent mean ± s.e.m.

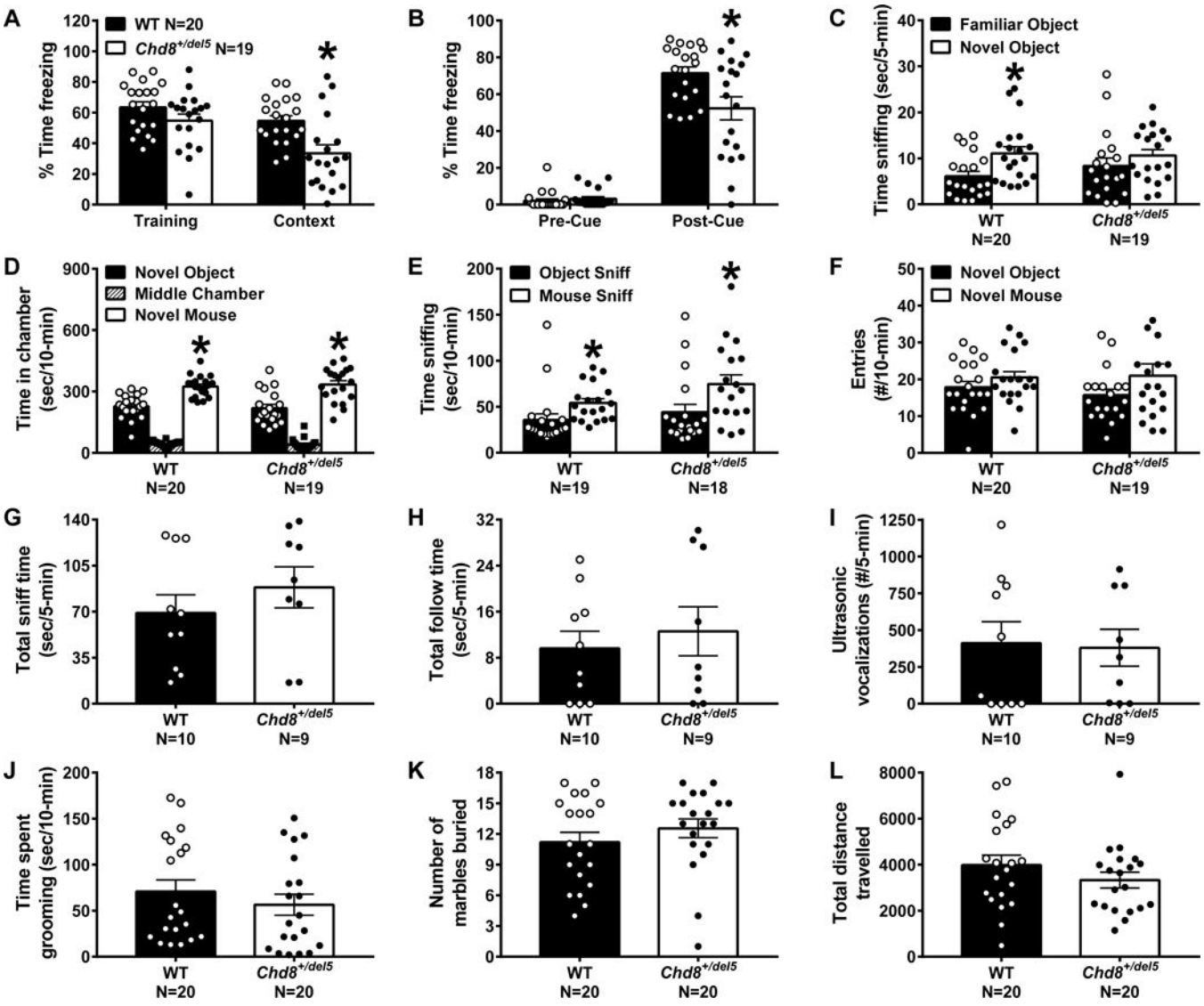

Figure 2. *Chd8*$^{+/del5}$ mice exhibit cognitive deficits but no ASD-relevant social or repetitive phenotypes

Fear Conditioning: Chd8$^{+/del5}$ mice exhibit deficits in learning and memory, including reduced freezing after tone-shock conditioning in both context (**A**; $t_{(1, 37)} = 3.3492$, *p = 0.0019) and cued assays (**B**; $t_{(1, 37)} = 2.7064$, *p = 0.0104). *Novel Object: Chd8*$^{+/del5}$ mice fail to show significant difference in exploration between a novel and familiarized object (**C**; WT $F_{(1, 19)} = 11.503$, *p = 0.0031; *Chd8*$^{+/del5}$ $F_{(1, 18)} = 3.2825$, p = 0.0867). *Three-Chamber Social Approach: Chd8*$^{+/del5}$ mice do not exhibit differences relative to WT littermates in (D) time spent in chamber with a novel mouse (**D**; WT $F_{(1, 19)} = 16.31$, *p = 0.0007; *Chd8*$^{+/del5}$ $F_{(1, 18)} = 9.744$, *p = 0.0059), time sniffing a novel mouse (**E**; WT $F_{(1, 18)} = 7.00369$, *p = 0.0164; *Chd8*$^{+/del5}$: $F_{(1, 17)} = 12.8051$, *p = 0.0023), or chamber entries (**F**; $F_{(1, 37)} = 0.11$, p = 0.73). *Male-Female Social Interactions: Chd8*$^{+/del5}$ mice exhibit no differences between WT littermates in time sniffing (**G**; $t_{(1, 17)} = 0.9409$, p = 0.3599), time following (**H**; $t_{(1, 17)} = 0.5785$, p = 0.5705), or ultrasonic vocalizations during interactions with an estrus female (**I**; $t_{(1, 17)} = 0.1634$, p = 0.8722). *Repetitive Behavior: Chd8*$^{+/del5}$ mice

do not exhibit any differences in time spent self-grooming (**J**; $t_{(1, 38)} = 0.8552$, $p = 0.3978$) or number of marbles buried (**K**; $t_{(1, 38)} = 1.0151$, $p = 0.3165$). *Open Field: Chd8*$^{+/del5}$ mice do not exhibit any differences in distance traveled (**L**; $t_{(1, 38)} = 1.1795$, $p = 0.2455$). All data shown from first cohort. Male mice were used in G-I; males and females were used in all other panels. Unpaired t-tests used for A-B, G-L; repeated-measures ANOVA used for C-E; one-way ANOVA used for F. Error bars represent mean ± s.e.m.

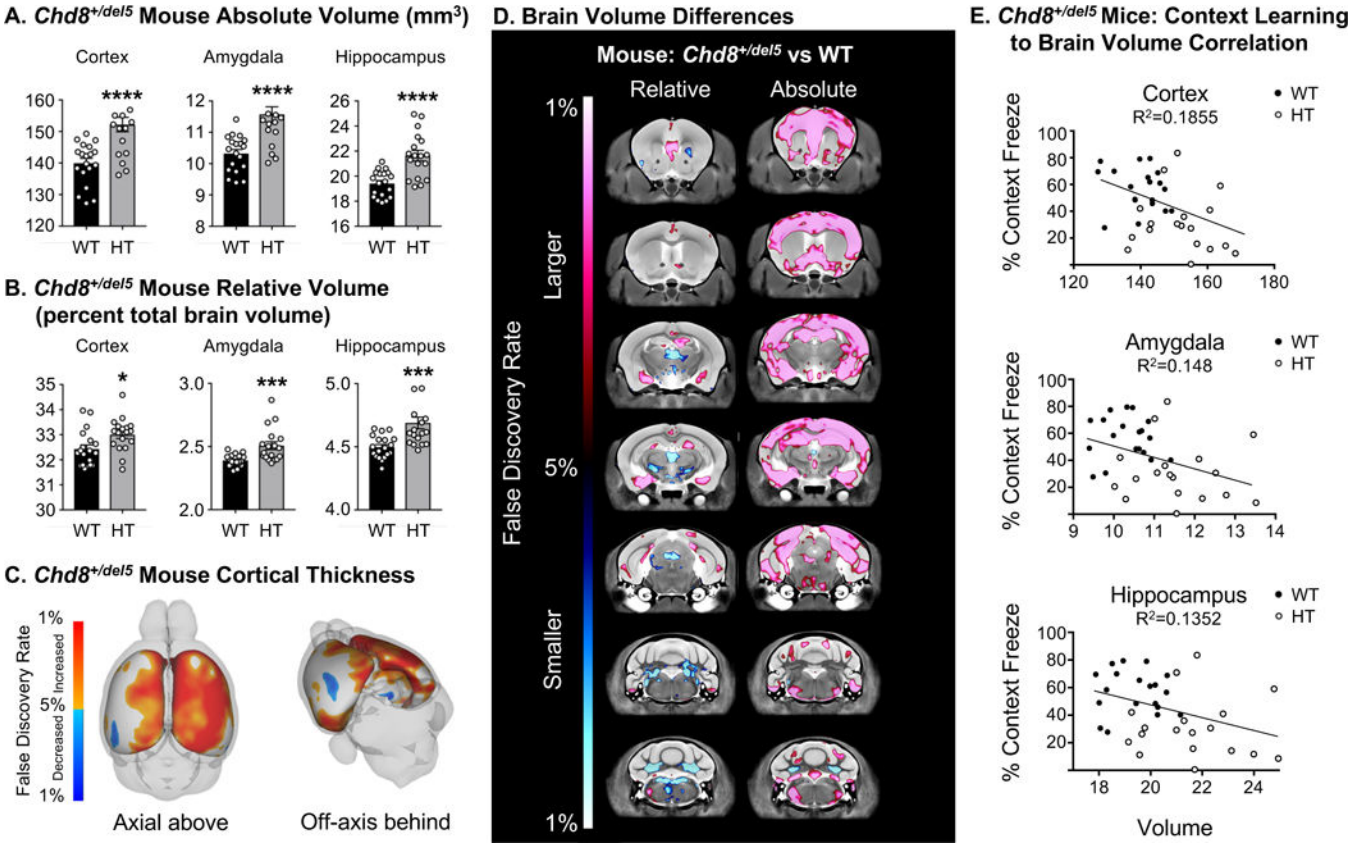

Figure 3. *Chd8* haploinsufficiency drives megalencephaly and cognitive impairment in mouse

A. MRI revealed significant increases in absolute regional volume of cerebral cortex (****p < 0.0001), amygdala (****p < 0.0001), and hippocampus (****p < 0.0001) in *Chd8*$^{+/del5}$ (HT) mice. n: WT = 19, *Chd8*$^{+/del5}$ = 18. See Table S1 for full regional statistical analysis and FDR values. **B.** Increases in volume are still significant for the cortex (*p = 0.00147), amygdala (***p = 0.0010), and hippocampus (***p = 0.0004) after correction for absolute brain volume. **C.** Increased cortical thickness is present in *Chd8*$^{+/del5}$ mice. **D.** Voxel-wise differences in volume between *Chd8*$^{+/del5}$ and WT littermates. **E.** Concordance of specific brain region size and cognitive impairment in *Chd8*$^{+/del5}$ mice (context conditioning score; R^2: cortex = 0.1855, hippocampus = 0.148, amygdala = 0.1352). Student's t-test used for A-B; error bars in A-B represent mean ± s.e.m.

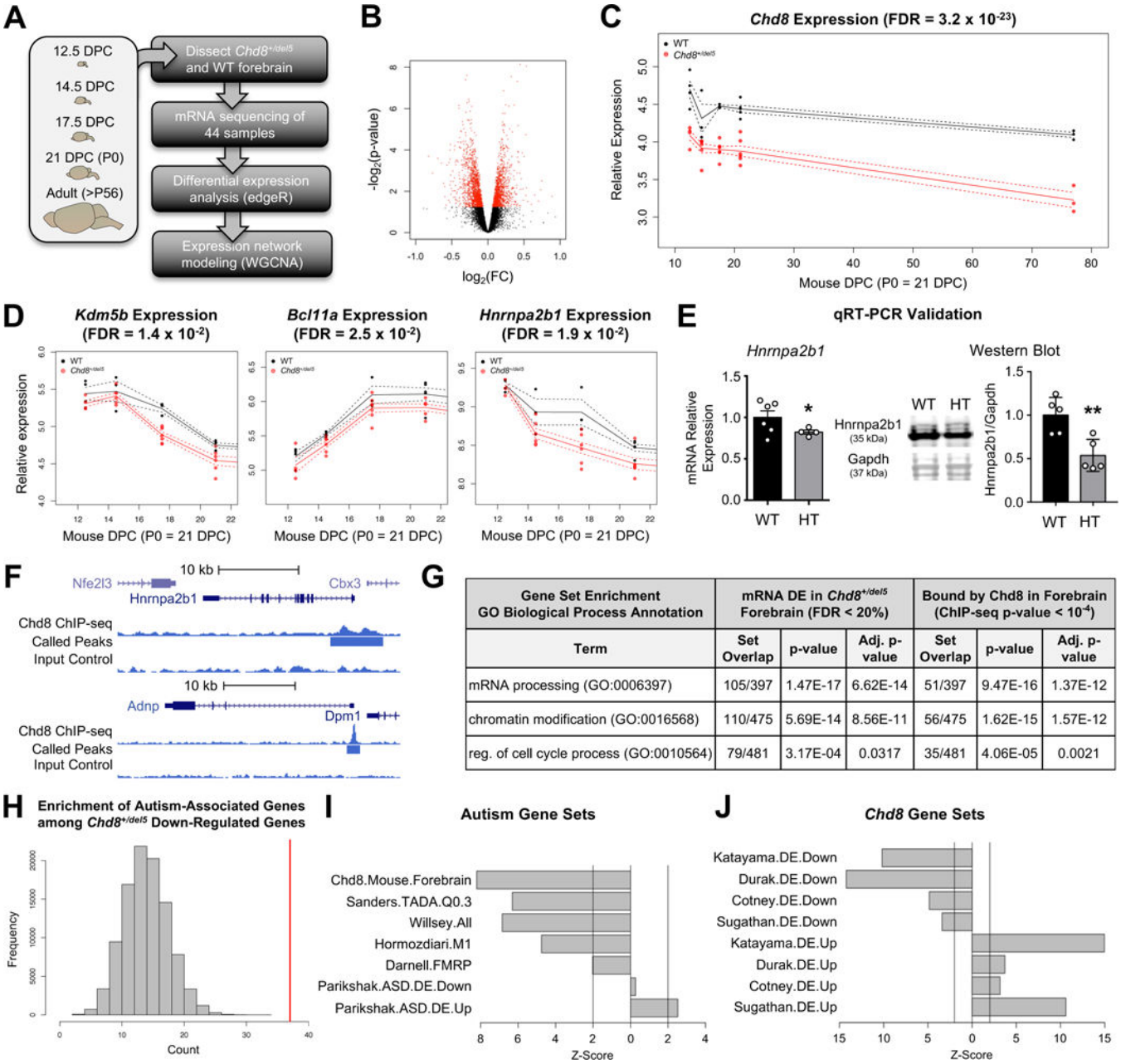

Gene Set Enrichment GO Biological Process Annotation	mRNA DE in *Chd8*$^{+/del5}$ Forebrain (FDR < 20%)			Bound by Chd8 in Forebrain (ChIP-seq p-value < 10^{-4})		
Term	Set Overlap	p-value	Adj. p-value	Set Overlap	p-value	Adj. p-value
mRNA processing (GO:0006397)	105/397	1.47E-17	6.62E-14	51/397	9.47E-16	1.37E-12
chromatin modification (GO:0016568)	110/475	5.69E-14	8.56E-11	56/475	1.62E-15	1.57E-12
reg. of cell cycle process (GO:0010564)	79/481	3.17E-04	0.0317	35/481	4.06E-05	0.0021

Figure 4. Differential gene expression in *Chd8*$^{+/del5}$ neurodevelopment

A. Schematic of our experimental pipeline. DPC, days post conception. **B.** Volcano plot showing that most DE genes (red) exhibit relatively subtle fold changes (FC). **C.** *Chd8* is the top differentially expressed gene; panel shows relative expression in *Chd8*$^{+/del5}$ and WT littermates across brain development. DPC, days post conception. **D.** Example expression patterns in *Chd8*$^{+/del5}$ forebrain of three DE genes across developmental stages. DE FDR shown for C-D. Solid lines, means; dashed lines, ± 1 s.e.m. **E.** Validation of DE expression of *Hnrnpa2b1* RNA (left; n: WT = 6, *Chd8*$^{+/del5}$ = 4) and protein (right; n: WT = 5, *Chd8*$^{+/del5}$ = 5) in *Chd8*$^{+/del5}$ (HT) forebrain at P0 (Student's t-test, RNA *p = 0.0248, protein **p = 0.0055). Error bars represent mean ± s.e.m. **F.** Chd8 ChIP-seq at *Hnrnpa2b1*

and *Adnp* loci. **G.** Representative significant GO terms for DE genes and for genes whose promoters are bound by Chd8. **H.** Enrichment of autism-associated genes (Q < 0.3 from Sanders et al. 2014[19], $p = 2.8 \times 10^{-10}$) in our DE gene set, based on randomly sampled gene sets (bars) versus observed number (red line). **I-J.** Comparison of DE down- and upregulated genes identified here with autism- and Chd8-associated genes. Directionality on x-axis represents test gene set used in analysis (left of zero: downregulated DE genes; right of zero: upregulated DE genes); z-scores generated via permutation test. Vertical lines at z-score = ±2.

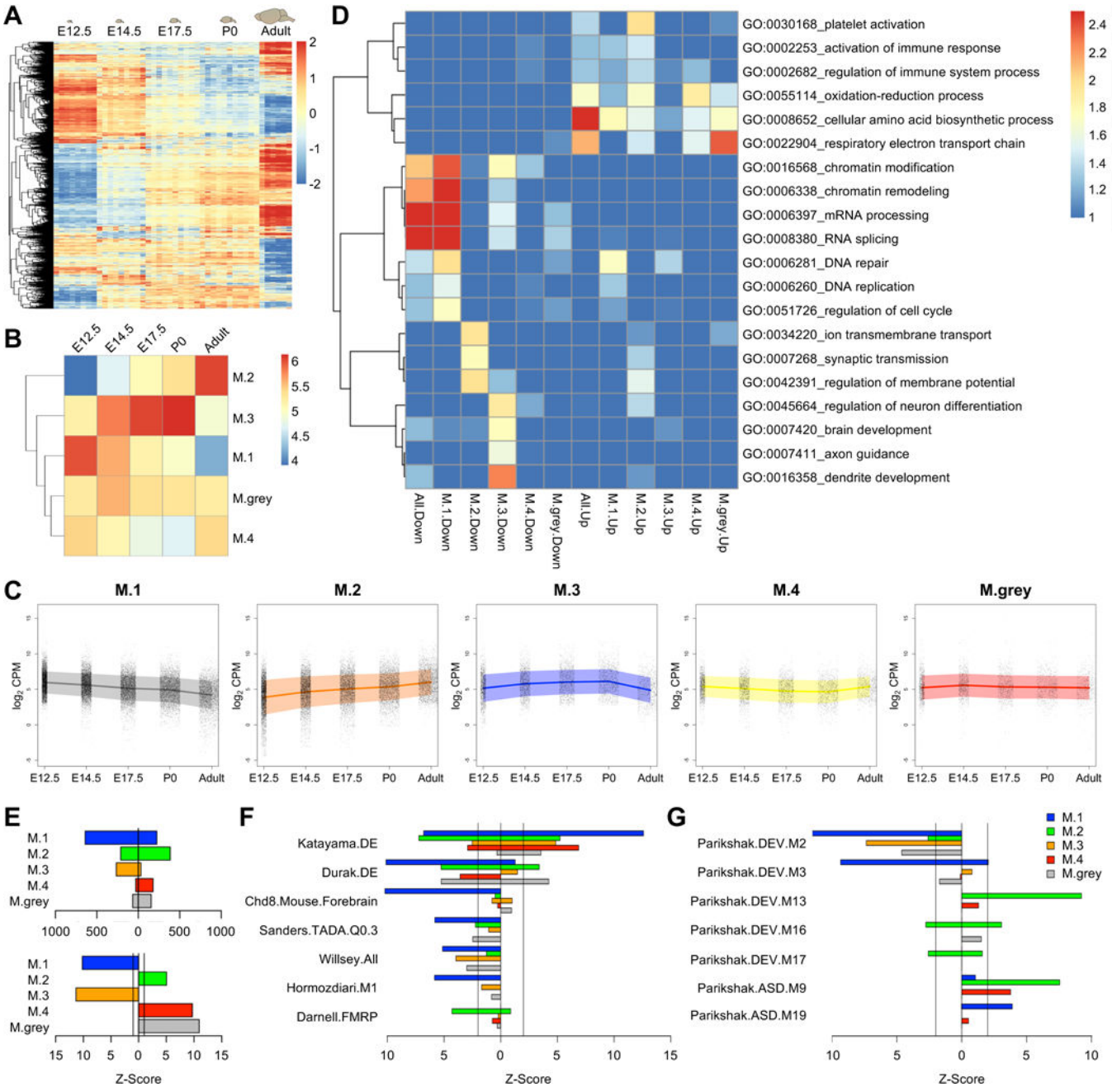

Figure 5. DE genes with correlated expression patterns across brain development reveal perturbations to early and later neurodevelopmental pathways

A. Heatmap representing expression of DE genes across all samples and stages. Scale bar: Z-score. **B.** Mean expression across developmental stages for the five developmental gene expression modules. Scale bar: mean log2(CPM) of module genes; CPM: counts per million. **C.** Gene expression plots for each module. Each plot shows expression for all genes in each module. Line represents mean, shaded area represents ± 1 s.d., and dots depict expression of individual genes. **D.** Functional enrichment of representative GO biological process annotations for DE genes. Scale bar: fold enrichment. **E.** *(Top)* Number of DE genes in each

module. *(Bottom)* Enrichment of down- or upregulated DE genes per module. **F-G.** Enrichment of autism- and Chd8-relevant genes within modules. In E-G, directionality on x-axis represents test gene set used in analysis (left of zero: downregulated DE genes; right of zero: upregulated DE genes); Z-scores generated via permutation test.

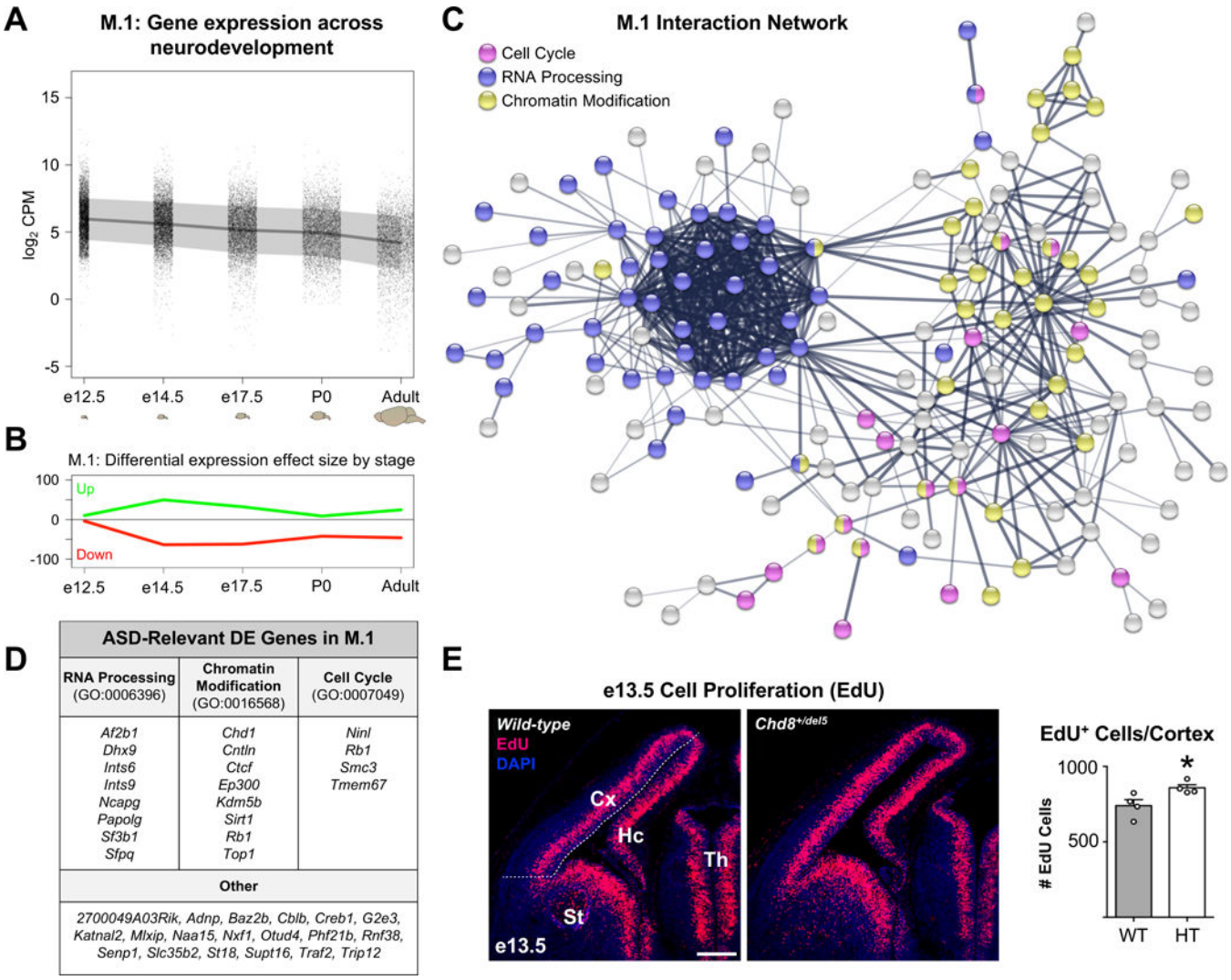

Figure 6. An early neurodevelopmental expression network (M.1) regulated by *Chd8* haploinsufficiency involved in chromatin modification, RNA processing, and cell cycle

A. M.1 gene expression plotted across brain development. Dots represent individual genes, line represents mean expression and shaded area represents ± 1 s.d. **B.** Relative mean differential expression of up- and downregulated genes in M.1 across brain development. **C.** STRING proteinprotein interaction network of M.1. DE genes are colored by annotation to GO biological process terms. **D.** ASD-relevant DE genes in M.1 associated with selected GO terms. **E.** *(Left)* Representative coronal sections of e13.5 brain stained for EdU (magenta) and DAPI (blue) in WT and *Chd8*$^{+/del5}$ mice (n = 4 mice each for both genotypes). Scale bar, 200 μm. Below white dotted line: measured neocortical area. *(Right)* Plot (mean ± s.e.m. with dots representing individual samples) of EdU positive cells per area. Student's t-test *p = 0.0388. Cx, cortex; HC, hippocampus; St, striatum; Th, thalamus.

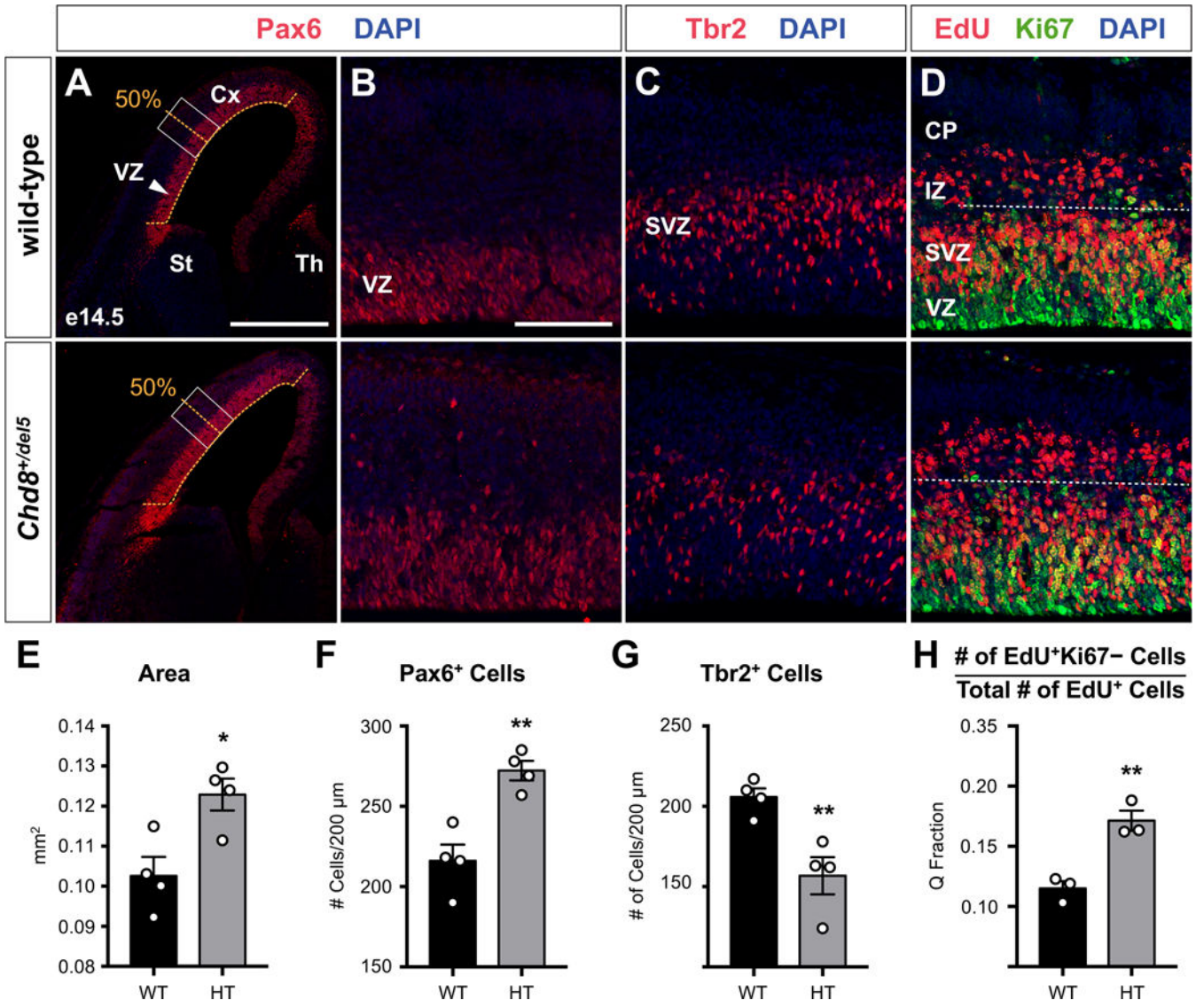

Figure 7. *Chd8*$^{+/del5}$ mutants exhibit altered cortical neurogenesis at e14.5

A-B. Immunofluorescent analysis of Pax6^{+} radial glial cells reveals an increase in the overall population as measured over the entire cortical hemisphere (**A**), quantified in **E**, and within midcortical 200-µm-wide segments (**B**), quantified in **F**. Scale bars, 500 µm in A and 100 um in B-D. **C.** Tbr2^{+} intermediate progenitors are significantly reduced, quantified in **G**. **D, H**. The rate of neurogenesis (Q-fraction), measured as a ratio of EdU^{+}/Ki67$^{−}$ cells positioned basal to the proliferative VZ and SVZ (**D**; dashed line) over all EdU^{+} cells within the same segment, is increased in *Chd8*$^{+/del5}$ mice (**H**; 20-h EdU pulse; **p = 0.0057). E-F: Quantifications of **A** (*p = 0.0165) and **B** (**p = 0.0032), respectively. **G**: Quantification of **C** (**p = 0.0086). Analyses performed at e14.5; n = 4 mice each both genotypes in E-G; n = 3 mice each for both genotypes in H. All statistics via Student's t-test. Error bars represent mean ± s.e.m. HT, Chd8$^{+/del5}$ mice; CP, cortical plate; Cx, cortex; IZ; intermediate zone; LV, lateral ventricle, Str, striatum; SVZ, subventricular zone.

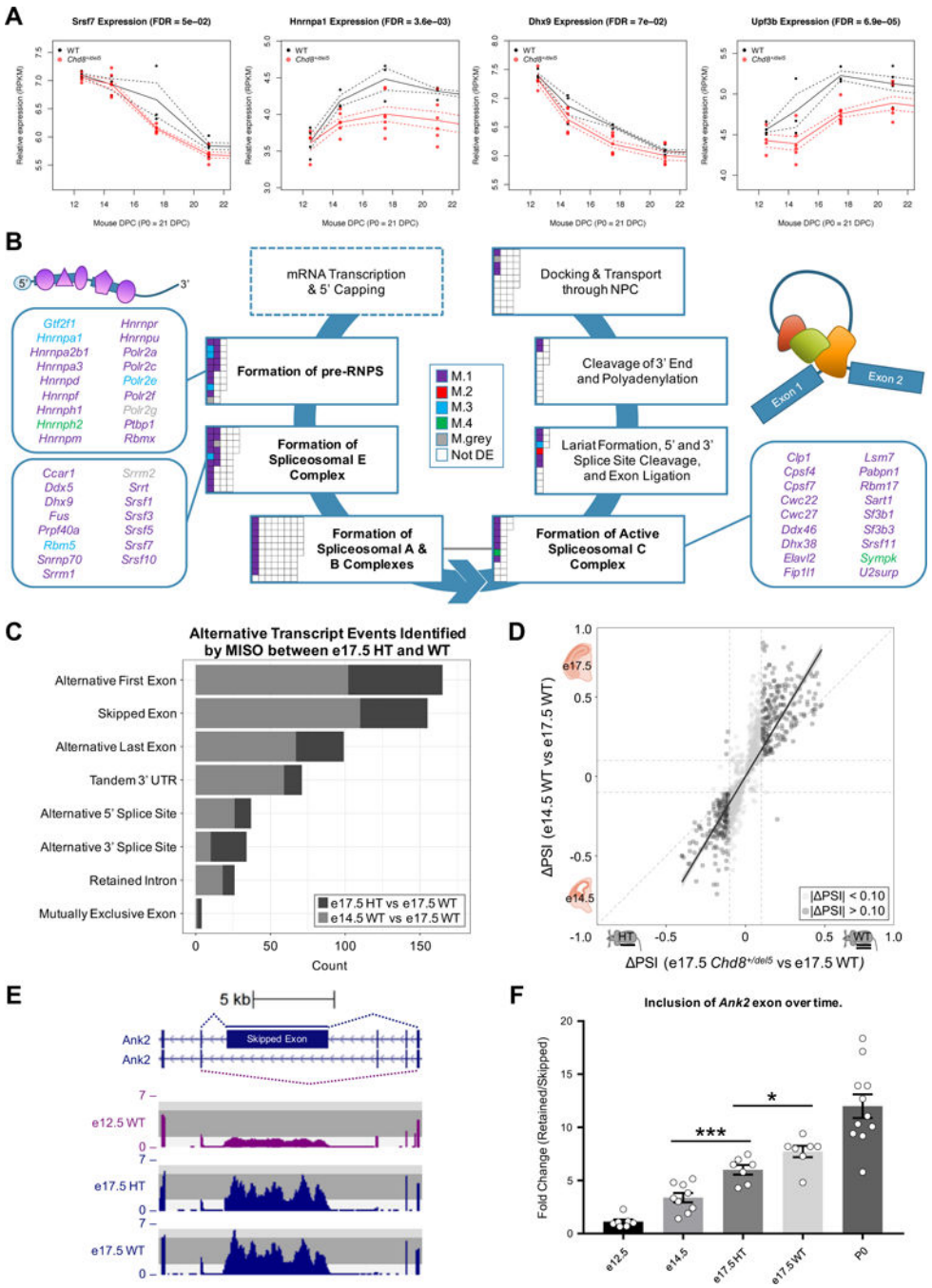

Figure 8. RNA processing pathways are enriched for differentially expressed genes in *Chd8*$^{+/del5}$ mice

A. Developmental expression of DE genes annotated to the formation of pre-mRNPs (*Hnrnpa1*), formation of the spliceosomal E complex (*Srsf7* and *Dhx9*), and lariat formation and 5' splice site cleavage (*Upf3b*). DE FDR shown; RPKM, reads per kilobase of transcript per million mapped reads. Solid lines, means; dashed lines, ±1 s.e.m. **B.** Schematic of the Reactome RNA processing pathways. DE genes in the pathways are denoted as squares colored by module. Each gene is represented once. Images depict simplified schematics of

nascent pre-mRNA (top left) and the active spliceosomal C complex (top right). **C.** We detected 591 differential isoforms (dark grey) detected by MISO between e17.5 *Chd8*$^{+/del5}$ and e17.5 WT brains. Of these, 393 isoforms are also differentially spliced between e14.5 WT vs e17.5 WT (light grey). **D.** Scatterplot of change in percentage spliced in (DPSI) of isoforms detected between e17.5 *Chd8*$^{+/del5}$ (HT) vs e17.5 WT (dark grey) and e14.5 WT vs e17.5 WT (light grey) comparisons, showing strong correlation between genotype and developmental events and direction of splicing change. **E.** Genome Browser representation of the alternatively spliced Ank2 exon (chr3:126,644,528–126,650,725). **F.** Isoform-specific qRT-PCR of the *Ank2* exon in WT and e17.5 *Chd8*$^{+/del5}$ mice. n: e12.5 = 7, e14.5 = 9, e17.5 *Chd8*$^{+/del5}$ = 7, e17.5 WT = 7, P0 = 11. Welch's t-test, e14.5 WT to e17.5 *Chd8*$^{+/del5}$; ***p = 0.001, e17.5 *Chd8*$^{+/del5}$ to e17.5 WT, *p = 0.03. Linear regression across developmental time points, adjusted $R^2 = 0.77$, $p = 4.53 \times 10^{-14}$. Error bars represent mean ± s.e.m.